Atmospheric CO$_2$ column concentration over Iran: Emissions, GOSAT satellite observations, and WRF-GHG model simulations

Samira Karbasi [a,b], Amir Hossein Abdi [c,d], Hossein Malakooti [b], Jose Antonio Garcia Orza [a,*]

[a] *SCOLAb, Department of Applied Physics University Miguel Hernandez, Elche, Spain*
[b] *Department of Marine and Atmospheric Science (Non-Biologic), University of Hormozgan, Bandar Abbas, Iran*
[c] *Friedrich Schiller University Jena, Faculty of Chemistry and Earth Sciences, Jena, Germany*
[d] *Max Planck Institute for Biogeochemistry, Biogeochemical Systems, Jena, Germany*

ABSTRACT

Regarding global warming and climate change, carbon dioxide (CO$_2$) is one of the most important greenhouse gases. Simulating CO$_2$ gas at hourly/weekly time intervals and desired vertical resolution is challenging due to the coarse horizontal resolution of global models. In this study, both column-averaged CO$_2$ mixing ratio (XCO$_2$) and vertical cross sections of CO$_2$ mixing ratio were simulated by the Weather Research and Forecast Green House gas (WRF-GHG) model at spatial resolutions of 30 and 10 km for the Middle East region as the first domain, and Iran as the second domain. Simulations consider the primary CO$_2$ sources (anthropogenic, biogenic, fire, and oceanic) and the Copernicus Atmosphere Monitoring Service (CAMS) dataset. XCO$_2$ retrieved from GOSAT satellite observations was employed to evaluate the simulation results of the column-averaged CO$_2$ concentrations in February and August 2010. The evaluations showed that the spatiotemporal variability of meteorological variables was well simulated by WRF-GHG with correlation coefficients r of 0.86–0.92, 0.67–0.75, and 0.76–0.82 for temperature, wind, and relative humidity, respectively, during February and August 2010. The evaluations also indicated that the WRF-GHG simulations outperformed the global model TM3, with mean bias error values of − 0.79 and 0.45 PPMV for WRF-GHG in February and August, respectively. The percentage contribution of net CO$_2$ emissions from human activities in Iran was calculated as (38.33 % and 23.70 %) of the total emissions, respectively, with values of 4.4 and 0.85 kg/km^2 in each month. The net emissions contributions of biogenic, fire, and oceanic sources were evaluated in February and August, with biogenic emissions contributing (31.901 % and 27.66 %), biogenic absorption contributing (24.07 % and 46.63 %), fire emissions contributing (5.7 % and 2.064 %), and oceanic emissions contributing (3.23 × 10^{-6} % and 2.23 × 10^{-6} %). Large-scale circulations and biogenic activity are responsible for the major features of the spatial and seasonal distribution of CO$_2$ in the area. In February, column mixing ratios are higher in more northern latitudes; in August, they are higher to the south. Furthermore, the simulated vertical cross sections show high CO$_2$ mixing ratios in the mid-lower troposphere and northerly/northeasterly advection in February; the vertical profile is inverted in August with high concentrations in the lower stratosphere associated with southwesterly advection. However, the interaction between the synoptic and sub-synoptic features with the topography determines the precise dispersion and distribution of CO$_2$. Despite the negligible emissions in central and eastern Iran, these factors play an important role in the observed concentrations in February and August. In August, the areas between the 120-day low-level monsoon flow of Sistan in eastern Iran, and the westerlies over western/southwestern Iran and the Zagros Mountain range, interact with the heat-low in the Iranian plains and with the Arabian subtropical high. In February, the dominant winds in western Asia were west winds, with the main source of pollution coming from the northeastern regions flowing towards central and eastern Iran. The equatorward displacement of the polar jet stream and the passage of low-pressure systems from the west in winter cause a temporary reduction in CO$_2$ concentrations.

* Corresponding author.
E-mail addresses: skarbasi@umh.es (S. Karbasi), abdi@bgc-jena.mpg.de (A.H. Abdi), malakooti@hormozgan.ac.ir (H. Malakooti), ja.garcia@umh.es (J.A.G. Orza).

1. Introduction

Global warming has captured worldwide attention. Atmospheric CO_2, as a key greenhouse gas, contributes to approximately 60 % of the total enhanced greenhouse gases effect and can impact the course of climatic changes. This will have serious implications for national security, global stability, and sustainable economic development (Jain et al., 2015; Liu et al., 2018; IPCC, 2021). Carbon dioxide is naturally produced in the Earth's atmosphere, acting as an essential nutrient for plants and a significant factor in the Earth's thermal balance (Jain et al., 2015; IPCC, 2021). According to the WMO Greenhouse Gas Bulletin, the global average atmospheric CO_2 concentration reached its highest level in 2020, at 413.2 ppm (Water, 2019). This value represents a 149 % increase in CO_2 levels compared to pre-industrial levels (before 1750). The CO_2 increase from 2019 to 2020 was slightly lower than the rise observed from 2018 to 2019 but higher than the average annual growth rate in the past decade. This value occurred despite a nearly 5.6 % reduction in fossil fuel CO_2 emissions in 2020 due to restrictions related to the coronavirus (COVID-19) pandemic. The National Oceanic and Atmospheric Administration (NOAA) Annual Greenhouse Gas Index (AGGI) indicates that from 1990 to 2020, the radiative forcing by long-lived greenhouse gases (LLGHGs) has grown by 47 %, with CO_2 accounting for approximately 80 % of this increase (WMO Greenhouse Gas Bulletin, 2020). Continuous and reliable observations of atmospheric greenhouse gases such as CO_2 are crucial for understanding the current global status of the carbon cycle, the spatiotemporal distribution of atmospheric CO_2, making reliable predictions of climate change behavior, controlling the emissions of these gases, and mitigating the effects of human activities on global warming.

A large number of ground stations have been established worldwide, utilizing methods such as bottle sampling, spectrometry, and eddy covariance to obtain concentration information on CO_2 and carbon flux (Liu et al. (2018). However, due to technical and financial constraints, the network of surface observation stations is not optimal and has limited regional-scale monitoring capabilities. In recent decades, with the development of remote sensing measurement methods, satellite-based observations have been adopted to cover some shortcomings of ground-based observations. The SCIAMACHY satellite, the first detector on the European Space Agency's (ESA) environmental research satellite (ENVISAT), was the first specialized space instrument to measure the atmospheric column-averaged CO_2 (hereafter XCO_2) mixing ratio (Bovensmann et al., 1999). The SCIAMACHY sensor is sensitive to the boundary layer height and has collected a large number of observations during its 10-year orbit. Despite its lower accuracy compared to current satellites, it still provides opportunities to study the behavior of the terrestrial biosphere and climatic changes (Wang et al., 2011; Barkley et al., 2007).

Currently, active satellites specifically conducting CO_2 observations include Japan's GOSAT, the United States' OCO-2, and China's Tan Sat. The objectives of these satellites are to provide global, long-term, and continuous monitoring of XCO_2 concentrations, improve measurement accuracy of carbon emission sources and sinks, as well as regional carbon dioxide concentrations, and enhance understanding of their distributional and evolutionary characteristics (Turner et al., 2015; Hakkarainen et al., 2016; Fischer et al., 2017). Satellite observations of CO_2, due to their global coverage and high measurement density, present new opportunities for enhancing this understanding. Despite having access to accurate and valuable satellite observation tools, simulating atmospheric composition, emissions, and transfers in Earth's atmosphere remains challenging.

Chemical transport models are extensively used for studying and predicting CO_2 on global and regional scales as well as for comparisons with observations (Xie et al., 2013; Wang et al., 2014). By combining atmospheric chemical transport models with CO_2 observations and meteorological variables, it is possible to address existing gaps in emission inventories and transport errors (Bloom et al., 2017). On the

other hand, use of CO_2 observations can be transformed into a direct and effective approach for identifying carbon sources and sinks (Peters et al., 2007; Peng et al., 2015; Tian et al., 2014). Since the model output is an estimate of the real world, its performance is limited by the accuracy of the input flux field and the transport mechanism of the model (Liu et al., 2018).

Since the 1990s, various global models have been used for simulating CO_2 concentrations (Patra et al., 2008). Most of these models were not only characterized by coarse spatial resolution, but some also lacked comprehensive meteorological parameterizations for accurately reconstructing atmospheric boundary layer processes or convection (e.g., Taguchi et al., 2011). In recent years, various models have been developed for simulating regional atmospheric composition transport with high spatial resolution (Sarrat et al., 2007; Peylin et al., 2011; Vogel et al., 2013). The WRF Greenhouse Gas (WRF-GHG) model has been developed for simulating the transport of inert tracers CO_2, CH_4, and CO (Beck and Joshi, 2015). To estimate CO_2, CH_4, and CO emissions and sinks, several flux models and emission inventories are employed.

The quality of the forward simulations largely depends on our ability to represent surface flux heterogeneity and model transport behavior around each site (Tolk et al., 2008). Recent studies using regional chemical transport models have reduced the limitations in horizontal model resolution, considered heterogeneity in surface fluxes, and hence resolved fine structures in greenhouse gas concentration changes (Meinshausen et al., 2017; MacLeod et al., 2020; Huang et al., 2021). However, CO_2 simulations using a regional model have not been previously conducted in the Iranian region. This article focuses on CO_2 emissions and atmospheric dispersion in the Iranian region. Iran is a unique area in the Middle East for conducting this study.

In this paper, we first introduce and examine CO_2 emission sources, GOSAT satellite observations, numerical simulation configurations, and validation of simulated CO_2 distribution using the Weather Research and Forecast Green House gas (WRF-GHG) model as a regional atmospheric chemical transport model and evaluate the accuracy of WRF-GHG simulation results. Then, we analyze the simulated CO_2 concentration field and the regional dispersion pattern of carbon dioxide greenhouse gas concentrations, identifying the most significant sources and distribution of emissions during both dry and wet months in relation to prevailing atmospheric circulations. In other words, this study discusses the distribution of simulated XCO_2, varying transport and atmospheric circulation, and long-range transport originating outside the simulation domain.

2. Materials and methods

2.1. Study region

The study area is Iran, a country in southwestern Asia with a highly diverse geography. Iran is the second-largest country in the Middle East, bordered by Armenia and Azerbaijan to the northwest, the Caspian Sea to the north, Turkmenistan to the northeast, Afghanistan and Pakistan to the east, the Persian Gulf and the Gulf of Oman to the south, and Iraq and Turkey to the west (Fig. 1). Iran's location between latitudes 25- and 40-degrees north places it in the southern part of the temperate zone of the Northern Hemisphere, and its longitudes between 44- and 63-degrees east have led to a diverse climate. It includes temperate and humid climate in the southern coasts and the Caspian Sea, cold climate in the western mountains, hot and dry climate in the central plateau, and hot and humid climate in the southern coasts .

The primary sources of greenhouse gas emissions of carbon dioxide and methane in Iran are various sectors of energy production (industrial processes, energy, agriculture and livestock, forestry, waste, etc.). The CO_2 emission data for the years 1970–2020 are going to be discussed regarding the relative relevance of IRAN as compared to other countries in Middle east.

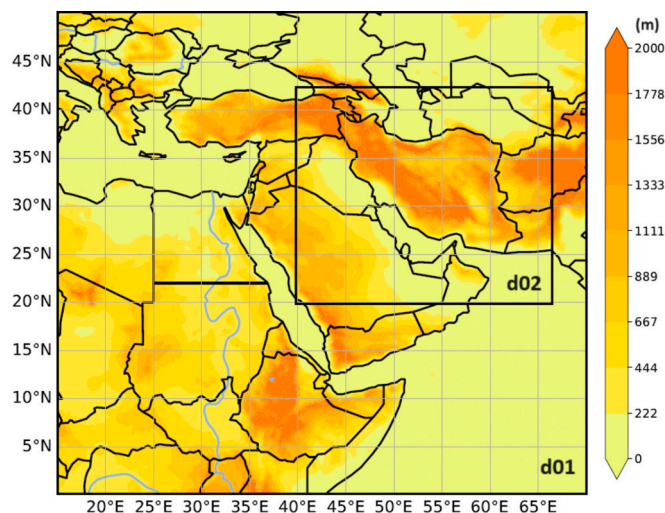The central region of the country comprises the Kavir and Lut plains.

Fig. 1. WRF-GHG simulation domains and topography of the study area from ERA5 data.

Table 1
Overview of WRF-GHG model configuration.

Schemes	WRF-GHG Options
Microphysics	WSM 3-class (Hong et al. 2004, MWR)
Radiation	Long Wave: RRTM (Mlawer et al., 1997, JGR)
	Short Wave: Dudhia scheme (Dudhia, 1989, JAS)
Planetary Boundary Layer	Mellor-Yamada-Janjic (Janjić, 1994, MWR)
Land Surface	Noah Land Surface Model (Chen and Dudhia, 2001)
Surface Model	Monin-Obukhov (Janjic) scheme (Monin and Obukhov, 1954)
Cumulus Parameterization	Monin-Obukhov (Janjic) scheme (Monin and Obukhov, 1954)
Chemistry	Grell-Freitas ensemble scheme (Grell and Dévényi, 2002)
Initial condition and boundary conditions	Greenhouse Gas tracer emissions
Time Period	CAMS (0.75^0), ERA5 (0.25^0)
Spatial resolution and domain grid points	d01: 30 km (173 × 124) d02: 10 km (222 × 213)
Time period	2010-02-01_00:00 to 2010-02-28_00:00 and 2010-08-01_00:00 to 2010-08-31_00:00
Time Step	d01: 180 s, d02: 60 s

In these areas, due to climatic conditions, population density, and the absence of air pollution sources such as refineries, greenhouse gas concentrations are expected to be lower than in other parts of Iran.

Since anthropogenic emissions have the largest share in the study region, we have examined the time series of anthropogenic CO_2 emissions from 1970 to 2020 for 10 countries in that region (Iran, Saudi Arabia, Iraq, Turkey, Afghanistan, Pakistan, Egypt, Oman, Yemen, and Kuwait). The Emissions Database for Global Atmospheric Research (EDGAR database), for the first time, includes estimates related to CO_2 emissions and removals due to land use, land-use change, and forestry sectors at the regional level. The main findings from the beginning of the 21st century indicate that global anthropogenic greenhouse gas emissions have been continuously increasing compared to the past three decades, primarily due to the growth of CO_2 "fossil" emissions by China, India, and other emerging economies (Crippa et al., 2023).

2.2. Model configuration

2.2.1. WRF-GHG

In this study, the WRF model version 3.9.1.1 is used along with the GHG module. As the aim of this research was to simulate CO_2 concentrations over Iran, the computational domains, as displayed in Fig. 1, were selected and defined. The study area consists of two nested domains, with horizontal grid dimensions of 124 × 173 and 213 × 222 points and grid spacing of 30 km for the outer domain (d01) plus 10 km for the inner domain (d02), respectively, covering the Middle East region and Iran. WRF uses the terrain-following hydrostatic pressure vertical coordinates (Skamarock et al., 2019). In this study, the model considers 37 vertical sigma levels with the top level at 65 hPa. To provide initial and boundary conditions for meteorological fields, ERA5 reanalysis data with a horizontal resolution of 0.25 degrees, 137 vertical layers, and 6-h temporal resolution were retrieved from the Copernicus Climate Data Store (CDS) using the CDS API. Copernicus Atmosphere Monitoring Service (CAMS) data were used for the initial and boundary conditions of carbon dioxide chemical fields in WRF-GHG (Massart et al., 2014). CAMS data is based on satellite observations along with ground measurements (Verkaik, 2019). CAMS provides CO_2 mixing ratios with a spatial resolution of 0.8 degrees on 137 vertical levels and a temporal resolution of 6 h (available at https://atmosphere.copernicus.eu). This study focuses on two different time periods: the dry season and the wet season in the study area, encompassing the simulated time intervals of February 1–28, 2010, and August 1–31, 2010. Table 1 contains all the details concerning the model configuration, the number of grid points, as well as the horizontal and vertical resolutions for both

domains, together with details regarding the numerical simulation conditions.

2.3. Emission data

The information related to the input emission data to the model has been obtained and studied from four different primary sources of carbon dioxide emissions on a global scale. Greenhouse gases originate from various anthropogenic sources, plus biogenic, biomass burning combustion, and exchanges with the ocean. In this section, a brief explanation of the different models and emission inventories used for calculating the CO_2 fluxes incorporated into the WRF-GHG model is provided.

For anthropogenic greenhouse gas emissions, the global EDGARv5.0 inventory is used among global datasets such as RETRO, REAS, EDGAR, NEI, and others. It includes the three main greenhouse gases (CO_2, CH_4, and N_2O) in each sector and country and is available online with a 0.1 by 0.1-degree resolution at the global level for greenhouse gases such as CO_2, CH_4, and other trace gases for the years 1970–2020 on an annual basis. The Emissions Database for Global Atmospheric Research (EDGAR) provides a comprehensive inventory of anthropogenic emissions from 1970 to 2020 for CO_2 and until 2018 for non- CO_2 greenhouse gases. A bottom-up calculation method based on the IPCC is applied for all countries; it demonstrates that consistent inventories can be developed for all countries with existing data quality constraints. EDGAR complements national inventories and reports prepared by the parties to the Paris Agreement. Solazzo et al. (2021) have also complements the EDGAR emissions inventory by providing an estimation of the structural uncertainty stemming from its base components and making assumptions regarding the cross-country uncertainty aggregation of source categories and they reported that the anthropogenic emissions covered by EDGAR for the combined three main GHGs for the year 2015 are accurate within an interval of −15 % to +20 % (defining the 95 % confidence of a log-normal distribution). According this study, although CO2 is responsible for 74 % of the total GHG emissions, CO2 has the least uncertainty within the EDGAR database, accounting for approximately 11 % of global uncertainty share.

The calculated emissions are interpolated hourly using the algorithm employed in the WRF-GHG model network. Anthropogenic CO_2 emissions are divided into four main sectors: residential, industrial, energy, and transportation. These emission data are used and adjusted over our domain, by applying spatial and temporal factors.

Regarding natural CO_2 emissions, Earth's carbon cycle studies have been conducted to better understand the major variables of the net

exchange between the biosphere and the atmosphere as well as to determine the amount of exchange between the atmosphere and the biosphere. The spatial resolution of global inverse simulations, which are commonly used to estimate the net biosphere flux, is rather coarse (Ballav et al., 2020). To introduce biospheric CO_2 emissions (net exchange between the biosphere and atmosphere), the NEE.ANN.CRUN-CEPv6 dataset has been used with a 0.5 by 0.5-degree spatial resolution on a daily time scale (Tramontana et al. (2016).

Fire is a complex biophysical process with multiple direct and indirect effects on the atmosphere, biosphere, and hydrosphere. Trace gas emissions and airborne particles from biomass burning are calculated using the Global Fire Assimilation System (GFAS) fire emission inventory (https://www.ecmwf.int/en/forecasts/dataset/global-fire-assimilation-system). The available data coverage is global, with a spatial resolution of 0.1 degrees and a daily temporal resolution. The accessible data covers the period from 2003 to the present.

The CarboScope (https://www.bgc-jena.mpg.de/CarboScope/) database in Jena estimates oceanic CO_2 fluxes based on various measurement methods (atmospheric CO_2 mixing ratios, partial pressure of CO_2 at the ocean surface). The dataset has been downloaded from the network with a spatial resolution of 0.5×0.4 degrees and a daily temporal resolution Takahashi et al. (2009).

2.4. GOSAT satellite

The Greenhouse Gases Observing Satellite (GOSAT), also known as Ibuki, was launched on February 23, 2009, from the Tanegashima Island in Japan (Kuze et al., 2009; Yokota et al., 2009; Parker et al., 2011). The GOSAT project is a joint effort of the Japan Aerospace Exploration Agency (JAXA), the Ministry of the Environment (MOE), and the National Institute for Environmental Studies (NIES) Miao et al. (2013). This satellite is the first specifically designed for monitoring CO_2 and CH_4 concentrations from space and orbits at an altitude of 666 km, synchronized with the sun, with equator crossing time of approximately 12:48 local time. The satellite's repeat cycle is three days. GOSAT is equipped with two sensors: (1) a thermal and near-infrared sensor for carbon observation featuring a Fourier Transform Spectrometer (TANSO-FTS), plus (2) a cloud and aerosol imaging system (TANSO-CAI) (Tables 2 and 3). With both TIR and NIR/SWIR sensors, GOSAT can observe both column amounts and vertical profiles of tracer gases. Estimates of global CO_2 and CH_4 distribution, as well as their spatial-temporal variations from emission sources, can be obtained Houweling et al. (2004).

2.4.1. GOSAT SWIR XCO2
Measuring atmospheric CO_2 concentration using space-borne instruments such as the Greenhouse Gases Observing Satellite (GOSAT) relies on observations of sunlight reflected from the Earth's surface and atmosphere.

Since 2013, five major algorithms have been developed by various research groups worldwide, focusing on processing GOSAT satellite data to retrieve the dry-air mole fraction of CO_2 (XCO_2) in global and temporal distribution with high spatiotemporal resolution. Column concentration retrieval algorithms for CO_2 column abundance from GOSAT observations include: the National Institute for Environmental Studies

Table 3
GOSAT TANSO-CAI Specifications (Yokota et al., 2009).

Band	Band1	Band2	Band3	Band4
Spectral coverage (μm)	0.370–0.390 (0.380)	0.664–0.684 (0.674)	0.860–0.880 (0.870)	1.56–1.65 (1.60)
Targeted substances		Cloud and aerosol		
Spatial resolution at nadir (km)	0.5	0.5	0.5	0.5

(NIES) algorithm from Japan Yokota et al. (2009), the RemoTec research algorithm from the University of Leicester Butz et al. (2009), the Carbon Cycle Modeling (SRON) algorithm from the joint Dutch Research Institute and the Karlsruhe Institute of Technology (KIT), and the Photon Path Length Probability Density Function (PPDF-D) algorithm developed at the NIES (Frankenberg et al., 2012; Oshchepkov et al., 2013). Each algorithm independently employs different methods for pre-processing and post-processing GOSAT satellite data to filter errors in regions affected by sunlight scattering. The operational NIES algorithm, used for regular processing of GOSAT radiance spectra, has been developed at the National Institute for Environmental Studies in Japan. The error in evaluations performed on the NIES algorithm products is less than 1 % compared to observations, with the complete implementation of this algorithm described by Yoshida et al. (2011).

2.4.2. Satellite observation for chemical validation
The performance of the NIES, ACOS, and Remo Tec algorithms was evaluated with GOSAT satellite observations over the mid-latitude region of the Northern Hemisphere (between 0 and 70 degrees of geographical latitude and 170 and 120 degrees of geographical longitude, respectively, east and west) for the years 2009 to 2021. It was determined that the NIES algorithm has a higher accuracy in the region of interest compared to the other two algorithms Karbasi et al. (2022). Accordingly, this study uses the Level 2 product dataset generated by the NIES algorithm to validate the simulations and statistical analysis of CO_2 column concentration from the WRF-GHG model at locations where remote sensing observations (GOSAT sensor data) are available. This evaluation is carried out for the periods February 1–28, 2010, and August 1–31, 2010.

The local overpass time of the GOSAT satellite is from 9:00 to 13:00; therefore, the simulated concentration values from the WRF-GHG model for this time are utilized in the analysis. To account for the spin-up time (training), the first 15 days of each simulation period are removed. Since the GOSAT XCO_2 satellite column concentration dataset is used for model evaluation, the simulated concentration values from the WRF-GHG model are also converted to column averages, and the monthly mean value at each point is considered.

2.5. TM3 model

The TM3 (Tracer Model 3) is an atmospheric transport model designed to simulate the distribution and transport of various gases and particles in the atmosphere. It is particularly used for tracing greenhouse gases such as CO_2, CH_4, and other long-lived gases at both global and regional scale available (Heimann and Körner, 2003). The model is usually run at different resolutions, ranging from $4° \times 5°$ to finer scales, depending on the requirements and computational power. In this study the nominal resolution has been used.TM3 incorporates a set of physical parameterizations to simulate transport, convection, and various chemical processes occurring in the atmosphere. It also models the exchange processes between the atmosphere and the Earth's surface, which impact the concentration of gases and particles.TM3 is especially used for simulating atmospheric flows and the transport of greenhouse

Table 2
GOSAT TANSO-FTS Specifications (Yokota et al., 2009).

Band	Band1	Band2	Band3	Band4
Polarization	P, S	P, S	P, S	–
Spectral coverage (μm)	0.758–0.775	5.56–14.3	1.92–2.08	1.56–1.72
Spectral resolution (cm^{-1})	0.2	0.2	0.2	0.2
Targeted gases	O_2	$CO_2 \cdot CH_4$	$H_2O \cdot CH_4$	$CO_2 \cdot CH_4$
FOV/FOV at nadir	IFOV: 15.8 mrad (corresponds to 10.5 km when projected on the Earth's surface)			

gases over long and short timescales. It allows researchers to study seasonal and annual variations in emissions and the distribution of gases. A primary application of the TM3 model is in climate change studies. However, like many atmospheric models, its accuracy depends on the quality of input data and the parameterizations used for physical and chemical processes. Additionally, the model's resolution and the computational power required for its execution can be limiting factors.

3. Results and discussion

3.1. CO$_2$ emission analysis

Table 4 presents the proportion of greenhouse gas emission sources in the study area for both the wet (February) and dry (August) months. The total emission of CO$_2$ greenhouse gases is divided into four main categories, including anthropogenic emissions, biosphere emissions, oceanic emissions, and fires. Further, Table 4 outlines the percentage share of each category in the total emission sources of greenhouse gases for both wet and dry months in the study area. Biogenic and oceanic uptakes are included in the table to allow a direct comparison of the relative relevance of each term in the CO$_2$ budget.

Among CO$_2$ emission sources, anthropogenic emissions are the largest contributor to CO$_2$ greenhouse gas emissions, with a percentage share of 38.33 and 23.7 in February and August, respectively. Biosphere emissions, following anthropogenic emissions, have a significant share in CO$_2$ greenhouse gas emissions. Biosphere emission sources consist of two main parts: uptake and emission, with the share of biosphere uptake at 24.07 and 46.63 in February and August, respectively, and that of biosphere emission at 31.90 and 27.66 in February and August, respectively. As expected, the share of absorption is lower in February than in August. In addition, CO$_2$ absorption in August is greater than anthropogenic emissions and lower than anthropogenic emissions in February, as expected. The contribution of fires and oceanic emissions (emission and uptake) to CO$_2$ gas formation ranked third and fourth in the overall CO$_2$ emission share, respectively, accounting for 5.7 and 2.064 % for fire emissions and $3.23 \times 10^{-6\%}$ and 0 % as well as 0 and $2.23 \times 10^{-6\%}$ for oceanic uptake and emissions in February and August, respectively.

Fig. 2 displays the monthly average spatial distribution of greenhouse gas emission sources (anthropogenic, biosphere, fire, and oceanic) in 2010 over Iran. Anthropogenic greenhouse gas emissions during the dry and wet months are negligible in the eastern and central regions of Iran, as these areas have minimal population density, activities, and industries. These emissions are more significant in Tehran, the capital of Iran, and most of Iran's western and southern regions, especially in the Khuzestan plain at the head of the Persian Gulf. Anthropogenic emissions in these areas are mainly due to industrial activities, energy consumption for heating in winter, energy conversion industries, and transportation. Anthropogenic emission sources for the CO$_2$ pollutant show a distinct seasonal cycle, with the highest values in February and the lowest in August, with a February share of 14.63 higher, due to the increase in energy consumption for heating in winter and the decrease in consumption in summer. Biogenic CO$_2$ shows an even more evident seasonal pattern, particularly in western Iran and other vegetated areas, with net biogenic CO$_2$ emissions in February and net biogenic CO$_2$

uptake in August (negative values in Fig. 2b). Forest and agricultural fires are more frequent in August, as confirmed by the MODIS's active fire detection data (not shown), resulting in higher CO$_2$ release than in February. Fig. 2 also shows that in February, the eastern Mediterranean and the northern Caspian act like sinks of CO$_2$, while the rest of the major water bodies in the region are either weak sinks or sources. In contrast, they are all CO$_2$ sources in August, especially the northern part of the Indian Ocean.

Since anthropogenic emissions have the largest share in the study area, this section examines anthropogenic emissions for the ten countries in the study region (Iran, Saudi Arabia, Iraq, Turkey, Afghanistan, Pakistan, Egypt, Oman, Yemen, and Kuwait) from 1970 to 2020. Fig. 3 includes a time series of anthropogenic emissions (EDGAR_ CO$_2$) from 1970 to 2020. We observe that fossil CO$_2$ emissions have declined in all industrial economies for all countries in 2020, with the latest data on CO$_2$ in 2020 clearly showing that the COVID-19 pandemic has affected human activities: globally, CO$_2$ emissions dropped by 5.1 % in 2020, breaking the upward trend observed in the past four years Crippa et al. (2023). It can be observed from the comparison between countries that Kuwait has had the highest per capita carbon emissions in recent years, followed by Oman, Saudi Arabia, and Iran in second to fourth places, respectively. This is associated with the presence of refineries and the use of fossil fuels. Afghanistan and Pakistan are also ranked ninth and tenth in carbon emissions.

To compare countries with different levels of development and population, per capita CO$_2$ emissions have been calculated separately for each country. According to Crippa et al. (2023), the highest emission factors for most pollutants in the energy sector were found in developing regions, such as Africa, Latin America, Indonesia, India, and the Middle East, while lower values were observed in industrialized countries (United States, Europe, Japan, Korea, and China).

Among the ten countries analyzed, Kuwait had the highest per capita CO$_2$ emissions in 1970, 51.34 t CO$_2$/cap/yr, reflecting the intensity of human activities associated with industrial development. However, CO$_2$ emissions in Kuwait decreased from 51.34 to 20.91 t CO$_2$/cap/yr between 1970 and 2020, equivalent to an average annual decline of 0.8 %. This reduction in CO2 emissions is most evident due to the country's high levels of per capita CO2 emissions in 1970 and the sharp decline in oil production (and thus emissions) in the following years due to political decisions related to tensions in the region before and after the Yom Kippur War in 1973, with a minimum in the 1979 energy crisis, but also due to the high concern for its own oil reserves since late 1971 relative to earlier estimates (Kondo, 2024). The later sharp decline in emissions (oil production) following Iraq's invasion of Kuwait and the Gulf War is well seen in the plot for Kuwait and Iraq. The latest smooth and continued decline in per capita CO$_2$ emissions, starting in 2005, is mainly related to population growth and reduced dependence on oil in favor of gas natural for electricity production (EIA, 2023); policies aimed at reducing dependence on the oil-based economy and improving efficiency in energy production and use in the industrial and urban sectors have contributed to this reduction (Crippa et al., 2023). Oman shows the second-highest level of anthropogenic CO$_2$ emissions among the countries considered. Oman and other developing regions have seen significant changes over time due to a higher share of residential activities and the release of more pollutants through fossil fuel combustion. The trend of CO$_2$ emissions in Oman increased from 10.13 t CO$_2$/cap/yr in 1970 to 16.9 t CO$_2$/cap/yr in 2020, equivalent to a 0.66-fold growth. The trend of CO$_2$ emissions in Saudi Arabia is similar to that of Oman, with an upward trend between 1970 and 2018 from 8.06 t CO$_2$/cap/yr in 1970 to 17.63 t CO$_2$/cap/yr in 2018. By 2020, the level of CO$_2$ emissions decreased to 16.96 t CO$_2$/cap/yr. The sectors with the highest share of fossil CO$_2$ emissions in Saudi Arabia are electricity production and other industrial combustion (Crippa et al., 2023).

After this group of countries, the next in order of per capita emissions is Iran. Anthropogenic emissions in Iran have increased by approximately 1.96 times from 1970 to 2020, equivalent to an average annual

Table 4

Monthly mean average of CO$_2$ emission budget sources, used in the study area of WRF-GHG.

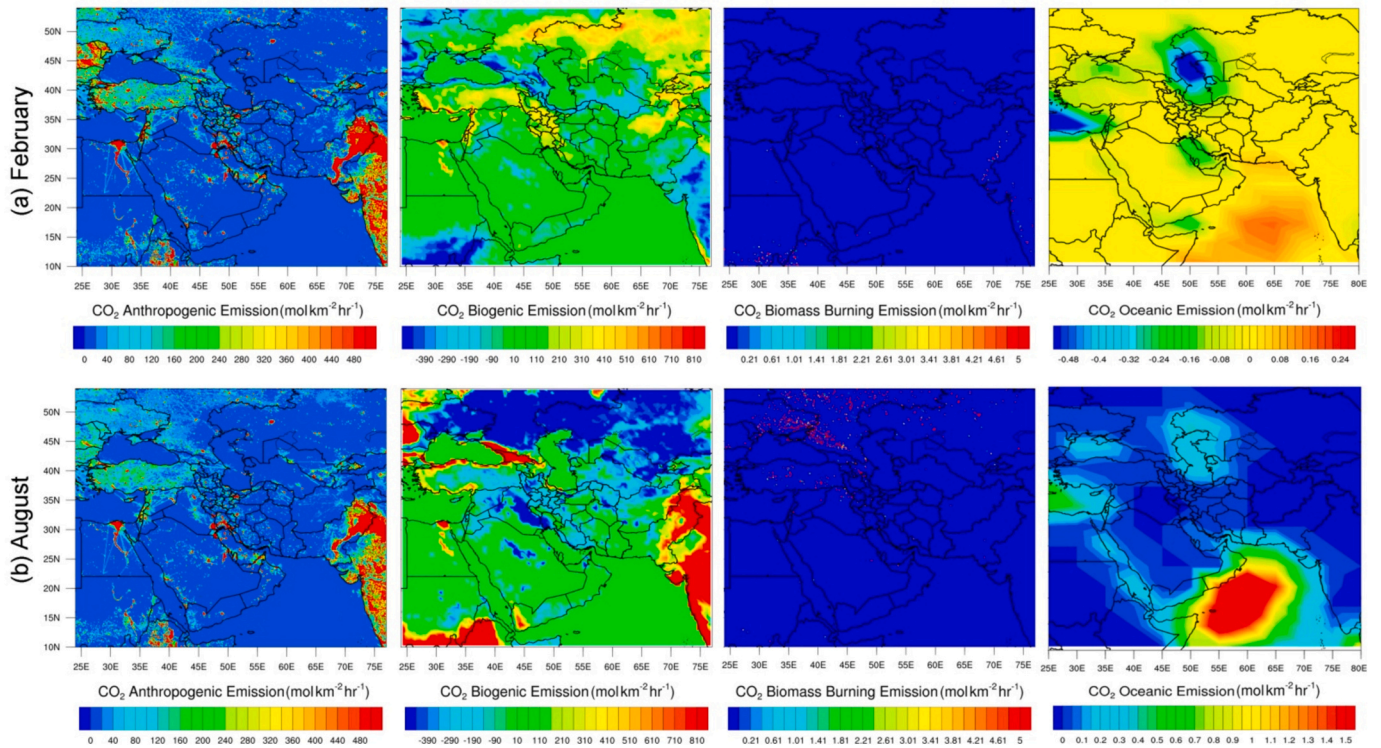| Emission sources-sink (mol/km^{2}hr)	February (%)	August (%)
Anthropogenic Emission	38.33	23.70
Biogenic Uptake	24.07	46.63
Biogenic Emission	31.90	27.66
Biomass Burning	5.7	2.064
Oceanic Uptake	3.23×10^{-6}	2.23×10^{-6}

Fig. 2. Emission budget of different CO2 sources (anthropogenic emission, biosphere emission, biomass combustion emission and oceanic emission, in mol/km2hr) as monthly averages. February (a), August (b), 2010.
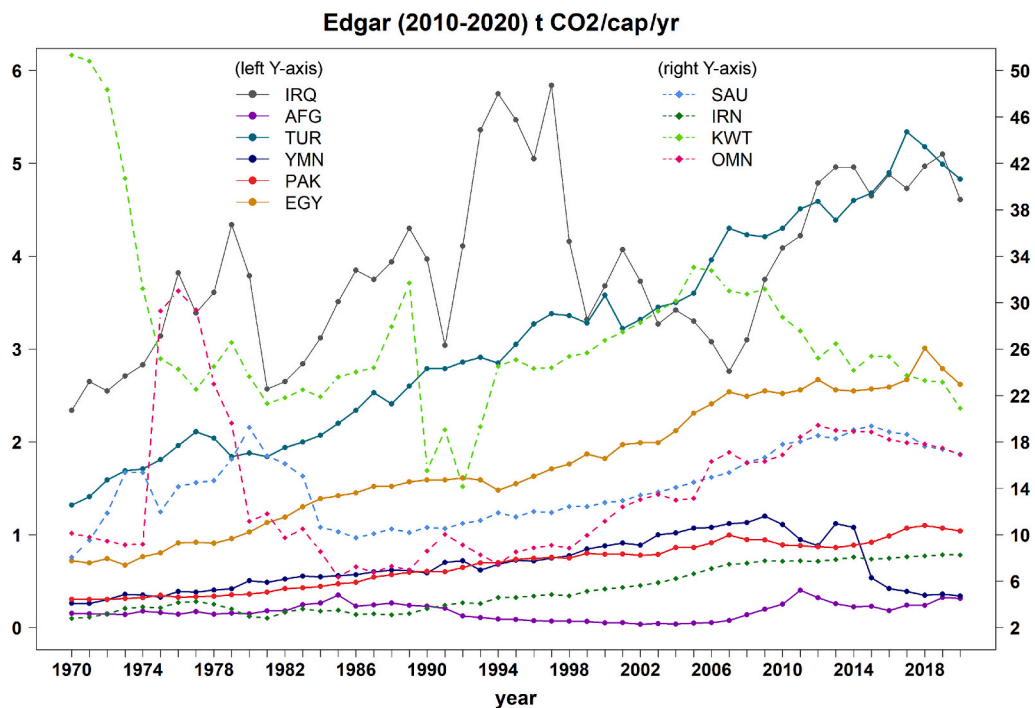

Fig. 3. Time series of per capita anthropogenic-induced emissions (EDGAR_CO_2 dataset (t CO_2/cap/yr)) from 1970 to 2020.

increase of 2.39 %. The value has risen from 2.79 t CO_2/cap/yr in 1970 to 8.26 t CO_2/cap/yr in 2020, indicating a shift towards industrial development compared to agriculture in greenhouse gas emissions since 1970. In Iraq, CO_2 emissions have risen from 2.34 in 1970 to 4.61 in 2020. Emissions decreased by 0.30 tons between 1990 and 2000 but then increased until 2020. The average increase in CO_2 emissions in Iraq

from 1970 to 2020 is 0.73 t CO_2/cap/yr, equivalent to an annual increase of 2.28 %. Turkey's CO2 emissions slowed their increase since 2007. The variations in emissions between 1970 and 2020 are 1.32 t CO_2/cap/yr and 4.83 t CO_2/cap/yr, respectively. The sectors with the highest share of fossil CO_2 emissions in Turkey include electricity production and other industrial combustion (Crippa et al., 2023). The trend

of anthropogenic CO_2 emissions in Egypt rose from 0.72 t CO_2/cap/yr in 1970 to 2.62 t CO_2/cap/yr in 2020, equivalent to a 1.96-fold growth or an average annual increase of 2.73 %.

The lowest annual emission values among the ten countries are in Afghanistan, Yemen, and Pakistan. CO_2 emissions in Afghanistan reached 0.31 t CO_2/cap/yr in 2020, compared to 0.15 and 0.23 in 1970 and 1990, respectively. The changes in CO_2 emissions from 1970 to 2020 are 0.15–0.31 t CO_2/cap/yr, 0.26–0.34 t CO_2/cap/yr, and 0.30–1.04 t CO_2/cap/yr for Afghanistan, Yemen, and Pakistan, respectively.

It is important to note that in all countries where the gross domestic product (GDP) has declined, greenhouse gas emissions have decreased at a relatively higher rate. In contrast, in low- and middle-income countries compared to high-income countries, the lack of pollution control equipment results in greater deployment of fossil and biofuels, leading to uncontrolled CO_2 emissions, primarily in the industrial sector (electricity production) and other industrial combustions.

Based on the results of EDGAR v6.1 for CO_2, this analysis underlines the overall robustness of the dataset, as it applies a bottom-up emission calculation method consistently across all countries globally, using a cross-sectional structure consistent with the IPCC's methods for greenhouse gas estimation. This approach allows for a comprehensive analysis of joint air pollutant reduction strategies.

3.2. Model validation

Values of spatiotemporal simulations of meteorological and chemical variables are extracted for two simulation periods and can be compared using various statistical methods. The statistical metrics used include mean bias error (MBE), mean absolute error (MAE), root mean square error (RMSE), and Pearson correlation coefficient (r).

3.2.1. Model validation – meteorological fields

Some errors in the simulation of CO_2 concentration are related to errors in the simulation of atmospheric meteorological variables. The sensitivity of atmospheric dispersion to wind fields and atmospheric turbulence, as well as the presence of some parameterizations of emissions in CO_2 simulation, which are functions of meteorological variables, are examples of the importance of this issue.

Three key meteorological variables, air temperature (AT), relative humidity (RH), and wind speed (WS), were chosen for the selected stations (a collection of cities including mountainous, coastal, and plain regions) from a set of synoptic meteorological station observations with appropriate spatial density (Fig. 4). Table 5 illustrates the evaluation metrics, including a comparison of simulated and observed variables for the selected stations, and summarizes the results for the evaluation period from February 1 to February 28 and August 1 to August 31, 2010.

Statistical parameters show that atmospheric fields and their daily variations have been well simulated. Based on the assessments, we have found that the 2-m temperature has the best r-values for both months at all observational stations. The correlation values of the 2-m temperature for every single station, range from 0.85 to 0.96 and from 0.80 to 0.89 for August and February, respectively, and the RMSE values (averaging 2.37 °C and 3.86 °C for dry and wet months, respectively) are small. The average mean bias error in the wet and dry months is −0.3 °C and − 0.54 °C, respectively. Following temperature, relative humidity has the best r-values in the wet month. r ranges from 0.76 to 0.88 during both months. Also, r-values in August are lower than in February for many stations. The mean bias error for relative humidity is −2.6 % and − 3.59 %, respectively.

Although the r-values for the 10-m wind speed are lower than those for relative humidity, its RMSE values are also low (averaging 2.29 and 2.91 m/s for wet and dry months, respectively). The average mean bias values are 1.29 and 0.82 m/s for the wet and dry months, respectively.

The model has been able to correctly calculate the temporal variations of surface temperature, relative humidity, and wind speed, to some
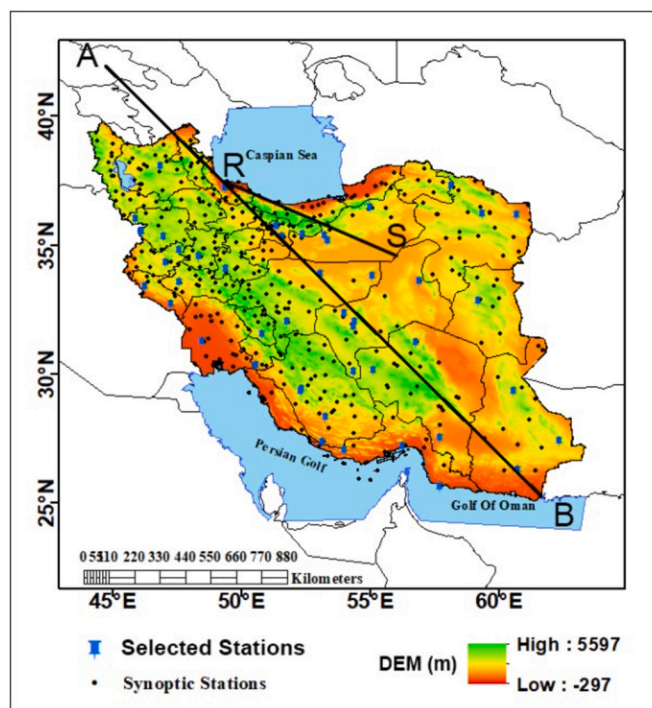

Fig. 4. Selected synoptic stations for meteorological validation. Digital elevation model of Iran (USGS/SRTM data, 30 m).

Table 5
Basic statistics of the comparison of meteorological parameters from WRF-GHG and synoptic observation stations (August–February).

Station Mean	Winter (Feb)			Summer (Aug)		
	RH (%)	AT (°C)	WS (m/s)	RH (%)	AT (°C)	WS (m/s)
Correlation (r)	0.82	0.92	0.75	0.76	0.86	0.67
Bias Error	−3.59	−0.38	1.29	−2.60	−0.54	0.82
RMSE	10.45	2.37	2.29	18.37	3.86	2.91

extent, with the calculated statistical errors for all measurements (Table 5 and Fig. 5). The general tendency of the model to underestimate temperature and relative humidity over the selected time period can be observed in Table 5.

Fig. 5 shows some overestimation of temperatures in the morning, and a clearer underestimation in the afternoon. These plots are time series averaged over all the synoptic stations studied, including mountain, desert and coastal environments. However, the data for each of the stations show this behavior more clearly (only a few days in the middle of February, when temperatures are below 0 degrees Celsius, show different behavior). Therefore, the ambient air in the model shows some sign of a faster warming in the morning and there is a faster cooling in the afternoon. This happens in connection with an overestimation in wind speed, which has been observed in other simulations in the region (Branch et al., 2021).

Several works have pointed out an overestimation by WRF of downwelling surface shortwave radiation (i.e., global incident radiation at the surface) in arid environments, leading to higher net radiation and sensible heating. This would explain the morning overestimation. Nevertheless, the positive wind speed bias can affect both the faster morning increase and the faster afternoon decrease with respect observations. The performance of the model is based in the interaction between different parameterizations, namely soil representation, planet boundary layer and radiation schemes (Table 1), which may account for
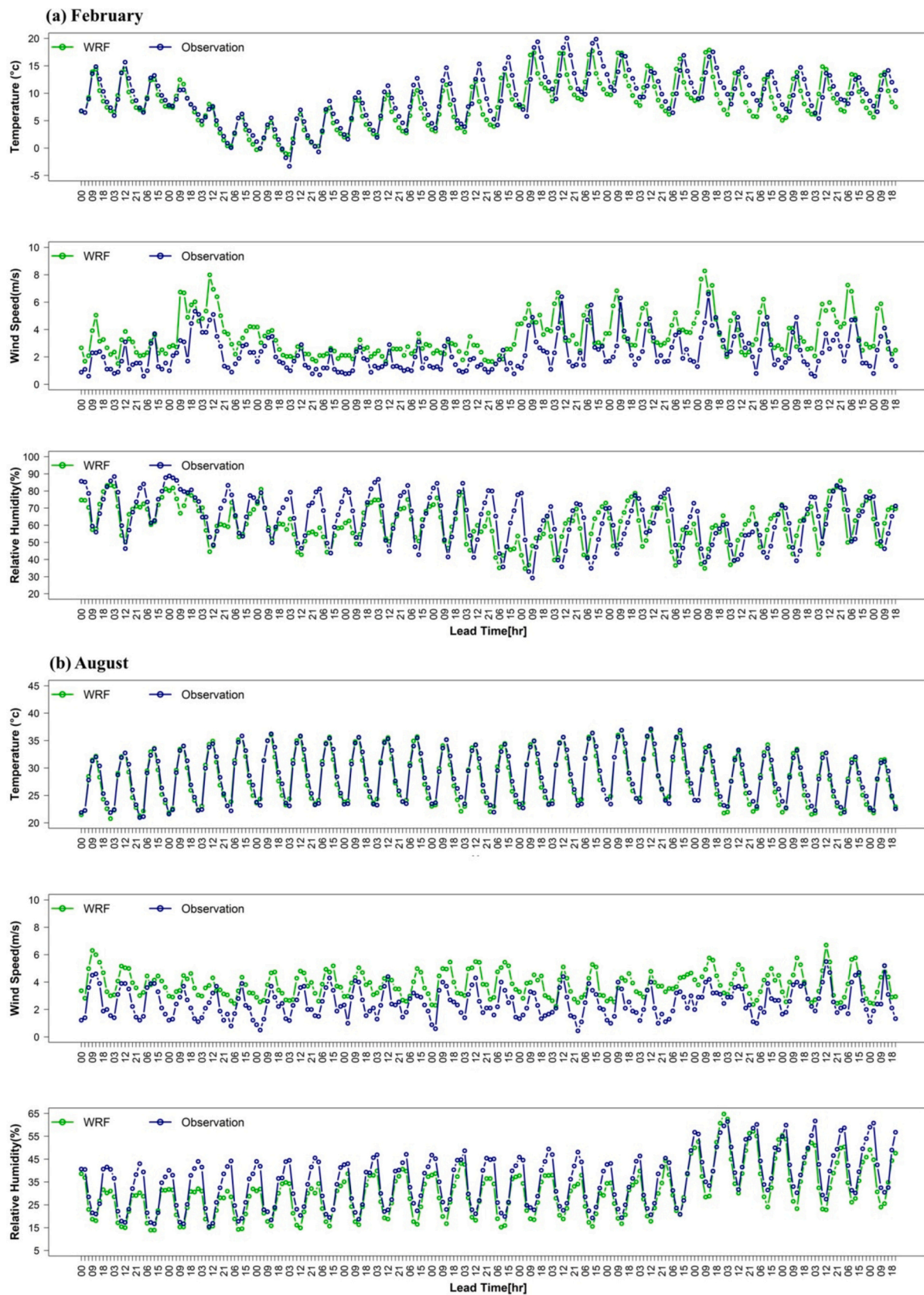
Fig. 5. Comparison of the three-hourly time series of the means over all the synoptic stations studied, of temperature (°C), relative humidity (%) and wind speed (m/s), observed and simulated by the WRF-GHG model for the months of February (a) and August (b).

the model biases. Therefore, these tendencies are part of the inherent complexities in modeling atmospheric processes, especially when dealing with diurnal variations. The slight deviations are within acceptable ranges, given the spatial and temporal scales the model operates on.

Fig. 5 also indicates that in both dry and wet months, simulated relative humidity is mostly underestimated in most areas, and a comprehensive examination of all 30 days in both months reveals that the model's values are closer to observations in August.

The predicted wind speed variations are consistent with the wind speed values obtained from measurements most of the time. Fig. 5 also indicates that, in most areas, the wind is overestimated.

3.2.2. Model validation – chemical fields

The WRF-GHG model output was both spatially and temporally interpolated over the GOSAT satellite measurement points to evaluate the model with various statistical parameters. This process was carried out for the warm season (August) and the cold season (February) data.

Table 6 presents the statistical evaluation results of the WRF-GHG model performance, along with the gas-phase chemistry mechanism GHG and the global TM3 model, in simulating carbon dioxide concentrations compared to the measured values obtained from the GOSAT satellite, and estimating the monthly average concentration for February and August.

Examining the error results (RMSE-MAE), it can be inferred that the WRF-GHG model represents reasonably well CO_2 concentrations regionally and performs better in cold seasonal conditions compared to warm seasonal conditions in the study area. The linear relationship is also good, with correlation coefficients between WRF-GHG XCO_2 and GOSAT XCO_2 that range from 0.71 to 0.87, the lowest value occurring in February and the highest in August.

There are several reasons for the discrepancy in the carbon dioxide mixing ratios obtained from numerical simulations and observations, one of which includes the uncertainty in the emission rates of pollutants of the EDGAR data base as input emission values in the model for the study area. Similarly, the uncertainty in the initial background values and boundary conditions created by CAMS data mainly due to short-term changes in local emissions, may lead to a rise in the CO_2 mixing ratio compared to the GOSAT observational data in the study area.

There are also errors and uncertainties in the simulation of atmospheric transport and dispersion by the WRF model associated with the parameterization of surface layer, boundary layer, and convection, which involve many approximations, and the selection of parameterization schemes is subject to debate.

The boundary layer plays a significant role in determining the column concentration. The simulation of carbon dioxide concentration within this section of the column is highly dependent on the thickness of this layer as calculated by the model. This calculation is often associated with considerable error, which tends to increase with greater boundary layer thickness, leading to a larger bias in the column concentration. The model is likely to perform better in winter because boundary layer thickness is typically thinner than in summer, resulting in less error

associated with thickness calculations, and therefore yielding more accurate simulations of the column concentration. Conversely, in the warm season, the impact of solar radiation is greater and daily temperature fluctuations are more pronounced. This creates additional challenges for the model in simulating temperature variations, as the intense diurnal changes can introduce errors in the thermal parameters of the model. Moreover, anthropogenic emissions are higher during winter (Fig. 2, Table 4) and more predictable, because of increased heating demands, so it is easier to capture and represent accurately in emission inventories such as EDGAR data base. This increase improves model accuracy by being in line with emission inventories that are often utilized in the models. The last reason is related to having less vegetation cover and also lower photosynthetic activity during winter compare to summer. Wintertime vegetation absorption of CO_2 is minimal and it simplifies the modeling, as the CO_2 levels are primarily driven by anthropogenic sources rather than a mix of natural processes.

In this regard, data assimilation techniques in simulations and the use of inverse modeling simulations can improve the performance of simulations and the quality of dispersion information. These techniques can help reduce uncertainties and improve the accuracy of the simulated results.

Table 6 also shows that the error values in the WRF-GHG model are lower than those in the global TM3 model, which is expected given the resolution of the global model and the interpolation of the global model data at GOSAT observational points.

3.3. Spatiotemporal distribution of XCO_2 from WRF-GHG and TM3 global model

Fig. 6 compares the spatial distribution of the column-averaged concentration (content from the surface to the top of the atmosphere) of simulated CO_2 from the WRF-GHG model, the analyzed information pattern, and the TM3 global model in the study area during the period of investigation (February and August). As observed, the WRF-CHG model is capable of simulating the spatial distribution of CO_2 for the monthly average in both dry and wet months. Additionally, there is minor difference in the representation of columnar CO_2 concentration distribution between the global model (TM3) and the regional model (WRF-GHG). Fig. 6a and b show a similar distribution of CO_2 in different parts throughout the study region, and the distribution also varies similarly by month. The average range of CO_2 concentration distribution is higher in the wet season (February) than in the dry season (August). In both February and August, the highest CO_2 mixing ratios are obtained in the northwest and western regions of the country. The spatial distribution pattern in August is similar to that in February, although areas with higher concentrations in February exhibit higher values. This distribution phenomenon may be related to winter warming and population distribution. In the central and eastern parts of the study area, there is a low population, resulting in less energy consumption for heating. The northern, western, and southwestern regions of the study area have a larger population, and thus XCO_2 is relatively high. The cities of Tabriz, Mashhad, Isfahan, and Abadan, following Tehran, are the most populous cities in Iran and have the highest carbon emissions for heating.

With the growth of vegetation cover in terrestrial ecosystems and the end of heating appliance use in August, the distribution of CO_2 concentrations in the northern and western regions rapidly drops, with the concentration range changing from 388 to 392.5 ppm in February to 386–389 ppm in August. Only in the western and northwestern regions do concentration values remain high, indicating that carbon emissions in these areas are heavily influenced by human activities.

Numerous potential explanations exist for the increase in CO_2 emissions in the Iranian region, one of which is the role of CO_2 emissions from biomass burning (wildfires). Excessive dry air, coupled with intense heat, leads to increased forest fires and, consequently, higher carbon dioxide emissions. However, due to the relatively small share of biomass burning in the total emissions budget (Table 4), it seems
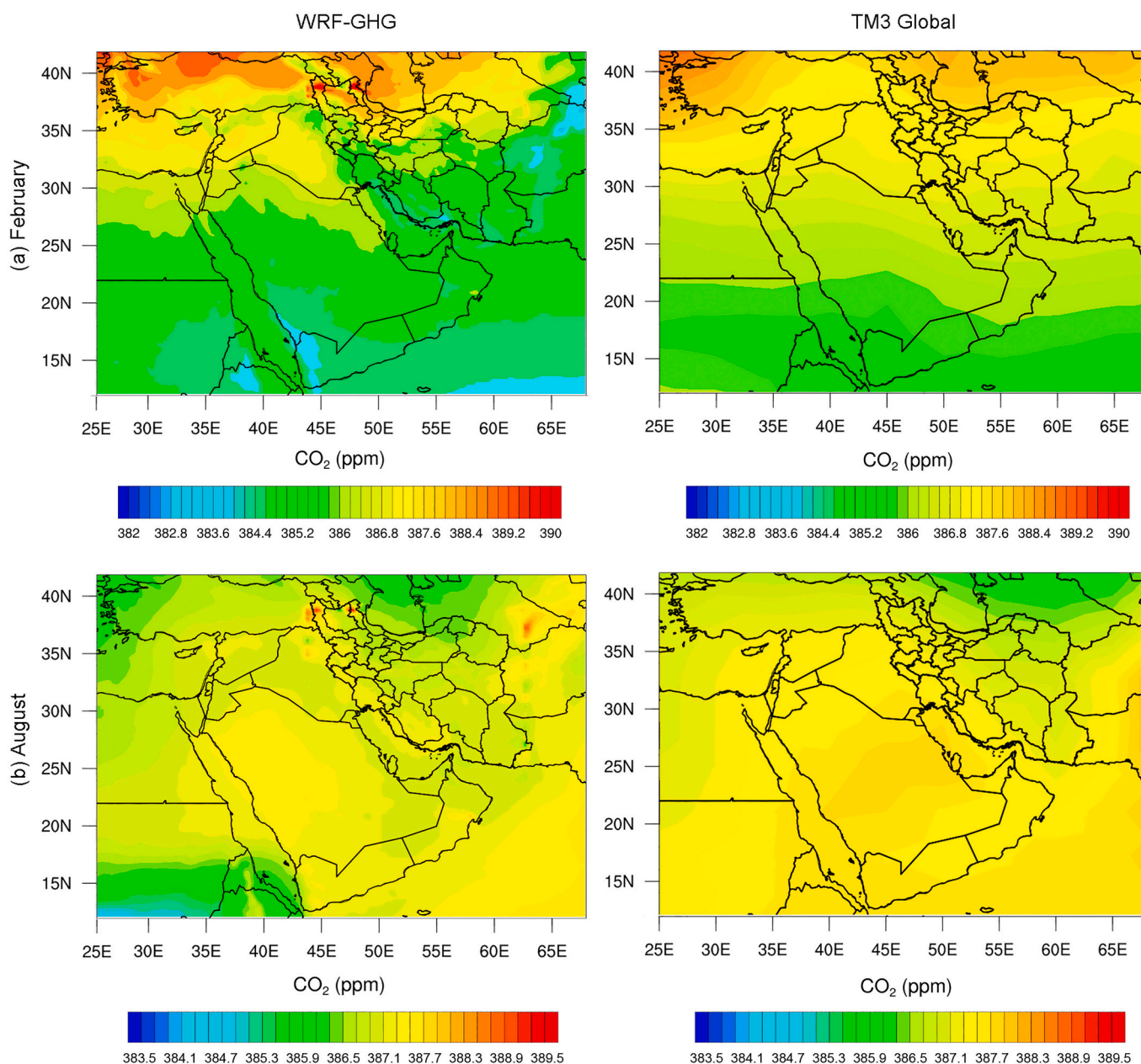
Table 6
Basic statistics of the comparison of XCO_2 Colum concentrations from WRF-GHG and TM3 with GOSAT.

Statistic Parameters	Period	Model	MAE	RMSE	MBE	r
CO_2 Error (ppmv)	2010.02.01–2010-02-28	WRF-GHG	1.43	1.63	−0.79	0.71
	2010.08.01–2010-08-31		1.81	1.96	0.45	0.87
	2010.02.01–2010-02-28	TM3	1.56	1.91	−0.85	0.24
	2010.08.01–2010-08-31		1.98	2.01	1.12	0.34

Fig. 6. Spatial distribution of simulated average column concentration of CO_2 by the WRF-GHG and TM3_Global models in (a) February and (b) August of 2010.

unlikely that the large increase observed in XCO_2 in August in the western regions of the country is due to a rise in biomass burning compared to the usual conditions for the region.

A different source that may explain the observed CO_2 distribution in this region is anthropogenic emissions from the extraction of fossil fuels. The western and southwestern regions of the country, due to exploitation of mineral resources such as oil and natural gas, which are known sources of CO_2 (Fig. 6), have emissions resulting from fossil fuel extraction recorded in the EDGAR emission database. However, these emissions are likely underestimated during the wet months.

Fossil fuel CO_2 emissions from EDGAR are used as an inventory of anthropogenic emissions in the model, based on the emission inventory published from each country to the United Nations Framework Convention on Climate Change (UNFCCC) in 2010. Results from simulations with greenhouse gas emissions by Scarpelli et al. (2020) indicate that growing emissions from fossil fuel combustion somewhat reduces the observed differences between simulations and observations. The

anthropogenic CO_2 emission inventory simulated in this study solely relies on the EDGAR v5 database as input for anthropogenic CO_2 flux and cannot adequately reproduce the observed XCO_2 mixing ratios by GOSAT for both dry and wet months.

Considering the statistical parameters in Table 6, we expect the difference in XCO_2 between WRF-GHG simulations and GOSAT to be partly due to underestimation of CO_2 emissions from fuel exploitation in EDGAR. This hypothesis aligns with several other studies that also show CO_2 emissions from fossil fuel extraction are underestimated by EDGAR (Miller et al. 2013; Massart et al., 2014). Another limitation of the EDGAR emission database is that it provides data only as annual averages. For future research involving CO_2 emissions, we recommend not solely relying on the EDGAR database but also using other inventories of pollutant emissions generated from fuel consumption.

Upon examining CO_2 concentration distribution in the study area, the eastern, central, and to some extent, southern regions show virtually no emission sources for CO_2; thus, the observed mixing ratios in these

areas can be considered as background values. In addition to the background concentration values in these regions, the crucial role of transport, reflected by the strong winds present in this area, should be mentioned. These winds are a significant factor in transporting emitted CO_2 eastward across the country. Another interesting pattern observed in this simulation is the role of orography. The influence of orography is substantial, and it appears that mountains cause recirculation and the formation of local circulation, hindering the transport of CO_2 and leading to restricted atmospheric dispersion, which results in accumulation and persistence of CO_2 in the same area.

3.4. Four-dimensional analysis of simulated CO_2

The central regions of Iran encompass the desert plains of Kavir and Lut and are bounded by the Zagros Mountains to the west and southwest and the Alborz Mountains to the north. Due to climatic conditions, low population density, and the lack of air pollution sources such as refineries in these regions, it is expected that, unlike other parts, greenhouse gases concentrations at lower levels would not be high. Despite this, as shown in Fig. 6, the central regions of Iran indicate 387–390 ppm of CO_2 concentration as an average for February and August.

In this section, we investigate the role of atmospheric dispersion, transport, and regional circulation of pollutants under the influence of the wind field on the observed concentrations in the central and eastern parts of the study area.

Fig. 6 reveals the monthly mean values of columnar CO_2 concentrations. As observed, during the dry month, the lower latitudes of the region experience higher concentrations. The primary sources of CO_2 for the study area are in western Iran and Saudi Arabia, with the other main sources being eastern Iran, the Tibetan Plateau, and the Indian Ocean.

Figs. 8 and 10 show the values related to the wind field and horizontal speed at 200, 500, and 850 hPa levels. The attempt to assess the impact of regional seasonal winds and investigate their activity in Iran using regional indices based on omega pressure tendency and horizontal wind speed spatially represents a simple and flexible method for studying regional circulation teleconnections.

Regional synoptic conditions in the summertime are influenced by the thermal low-pressure system extending up to the 700 hPa level, capped by high pressures over southern Saudi Arabia and western Iran. The Indian monsoon activity is observed in the southeastern region. The interaction between the heat-low system and the Indian monsoon results in a 120-day northerly low-level wind system in Sistan, in the east of
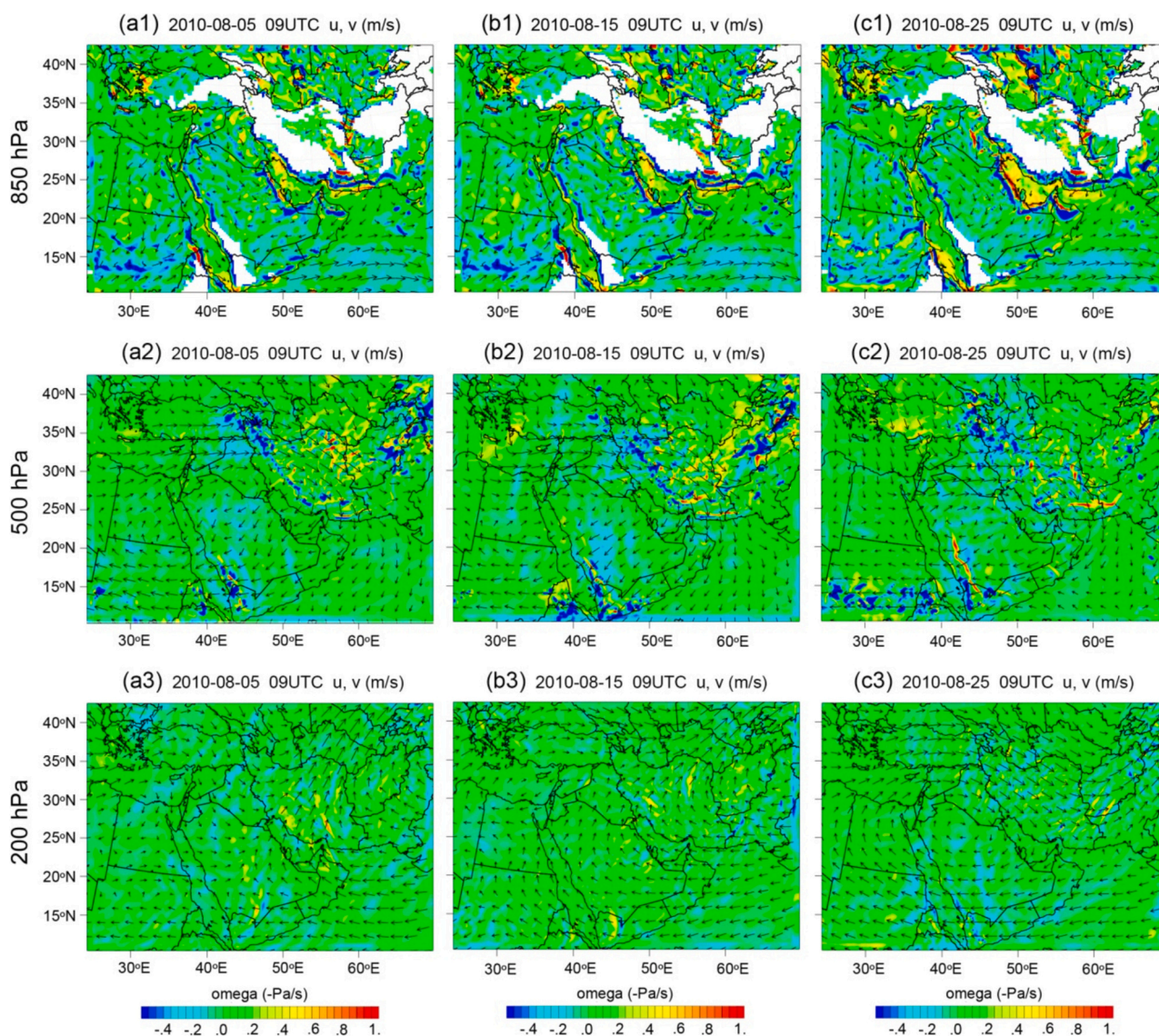

Fig. 7. Omega (-Pa/s) and horizontal wind at 850 hPa, 500 hPa, and 200 hPa on August 5, 15, and 25, 2010 (a, b, c). Blue (red) colors denote subsidence (ascent). (For interpretation of the references to color in this figure legend, the reader is referred to the web version of this article.)

Iran; the interaction between the heat-low and the subtropical high in Saudi Arabia creates the summertime northwesterly winds to the west of the Zagros Mountains and northeasterlies to the east of the mountain range.

In the analysis of synoptic conditions in August 2010, the days 5, 15, and 25 of August were selected instead of the monthly mean pattern. Fig. 7 shows the low-level wind field, the mentioned 120-day seasonal winds of Sistan, and the north summer monsoon are depicted in all three sea level pressure maps for these three times. Additionally, on the Arabian Sea, the southwest monsoon wind passing the equator and originating from the Mascarene high pressure, which is responsible for transporting moisture to the Indian monsoon, has been simulated well. The horizontal circulation of the wind field exhibits an anti-clockwise rotation (thermal low-pressure) over Iran and a clockwise rotation (high-pressure) over the Arabian Peninsula, which can be easily identified.

In the wind circulation fields in Fig. 7, it can be observed that (except for to the middle of the month, due to temperature drop and sedimentation) there is air descent in the southern and central regions of Iran. Central Iran experiences upward air movement under the heat-low 0.55–0.85 (-Pa/s). Areas involved in air descent have a higher potential to provide larger column CO_2 concentrations than areas experiencing upward air movement.

Following the seasonal solar inclination cycle, the structure of the Hadley cell and its descending branches move towards the north during the summer of the Northern Hemisphere, forming a coverage area of descent that extends from the central Mediterranean to Iran. The descent is always stronger in the winter hemisphere. The weakening of the average descent in a region in the Northern Hemisphere during the summer is greater compared to the weakening observed in the Southern Hemisphere during the summer of Australia, which is due to the opposing upward processes related to seasonal atmospheric activity at latitudes up to 40 degrees north (Tyrlis and Lelieveld, 2013).

The summer circulation situation is described by examining the vertical cross sections in Fig. 8 of the u-w vector and the vertical velocity w along the transect (A, B) in Fig. 4. It shows the geographic longitude and latitude of the main regions of ascent and subsidence. Climatic conditions in July coincide with the peak activity of the Indian monsoon and its stronger influence on the geographical latitude of the Arabian Sea and southeastern Iran. During the remaining period of July–September, away from the main monsoon activity, climatic conditions are similar but accompanied by gradually descending amplitudes.

Generally, in the middle of summer, the proposed "Walker-type" circulation in the ascending and descending regions is located in the southern position of the monsoon ascent compared to the subsidence regions of the Mediterranean and Iran. A semi-diurnal tropopause slope, with some of the highest observed subsidence values, leads to summer subsidence over the eastern Mediterranean and Iran (Tyrlis and Lelieveld, 2013). This regional subsidence represents significant deviations from the regional average and its seasonal speed (and even from neighboring areas such as the western Mediterranean), which cannot be solely attributed to Hadley circulation.

Subsidence over the Persian Gulf weakens from June to July with a northwestward expansion. By analyzing the horizontal wind field (from the ERA 5 horizontal wind dataset) in August, as well as the vertical cross sections displayed in the figure, it can be observed that this occurs from August 1 to 5, despite the high-pressure wind prevailing in northwestern Iran, which reduces the transport of pollutants from the east and west into Iran. Winds are northwesterly in eastern Iran and northwestern Iran (Fig. 7-a1, a2, a3) and (Figure 8_a_right).

The passage of low pressure from the northwest of Iran on February 16 weakens the lower-level jet stream (north wind in the northwest of the country and Sistan wind in the northeast), allowing the transport of pollutants from the west of the country (Figure 7_b1, b2, b3) and (Figure 8_b_right).

From February 21 to 27, with the presence of a high-pressure system from the higher latitudes to the north of the country, climatic conditions lead to a decline in the penetration of pollutants from the west and east of the country (Figure 7_c1, c2, c3) and (Figure 8_c_right).

Starting on February 27, a low-pressure system entered the country from the west. Still, in the last days of the month, the concentration in the western region of Iran (Arabia) was not as severe as in the early days. However, the passage of the low pressure again caused a change in wind direction and allowed pollutants to penetrate from the east of the country. The wind direction in the west of the country became westerly, and in the east, it became easterly again. The impact of topography is also important as it drives the lower-level and large-scale background features. On the one hand, the high-level surface warming on highlands contributes to the formation of mid-level cyclonic and anticyclonic centers during the summer, mainly in northwest Africa, central-west Saudi Arabia, and the Zagros Mountains. This leads to a rise in northerly flows and, thus, more intense subsidence in the eastern Mediterranean and Iran (Tyrlis and Lelieveld, 2013).

The Alborz Mountain range, which extends from Turkey to Iran, blocks the northerly flow and contributes to further warming on its dry side. Thus, the topography of the northern regions of Iran plays a significant role in shaping the subsidence towards the south of the mountain range axis. In the upper troposphere and lower stratosphere, the very large extent of the observed subsidence in the EMME region is related to the air coming from South Asia (Tyrlis and Lelieveld, 2013).

Based on the analysis of February, as observed in Fig. 6, the northern latitudes of the Caspian Sea have higher concentrations. In this month, the dominant winds in the region are westerly, and according to the dispersion analysis, the main sources of CO_2 are higher latitudes above the Caspian Sea and northeastern areas.

As observed in Fig. 9, the development of the seasonal wind impact on the summer climate of the Eastern Mediterranean and the Middle East (EMME) region expands the subsidence associated with the descending branch of the Hadley cell over the geographical latitude band 15–30 degrees N during the northern winter (Tyrlis and Lelieveld, 2013).

The synoptic conditions in Iran during January and February are influenced by the penetration of the polar jet into the middle latitudes and the passage of western low-pressure systems. In other words, the region is under the influence of the Ferrel cell circulation. The passage of a Mediterranean low-pressure system will accompany the regional ascent of air in its leading edge; additionally, horizontal wind speed will experience a significant growth, as can be observed in the sea-level checked contour maps in Fig. 10 and during the first week of February 2010.

Under these conditions, the ascending and descending air regions, particularly in southern Iran, possess high power, which is also influenced by the region's topography. The horizontal speed of the air ascent over Iran becomes more uniform.

As observed, from the first to the fifth of February, the concentrations at higher latitudes are not very high, and the main winds and currents are easterly, with no transfer of CO_2 to lower latitudes. It can be seen that the winds are westerly in the western Caspian Sea, while in the region from Rasht to Semnan (transect R, S in Fig. 4) they have a northwestern direction (Figure 10_a_right).

In mid-February, from the 13th to the 19th, the passage of a low-pressure system over higher latitudes causes the winds over the Caspian Sea to shift southward. The presence and movement of this low-pressure system in the region prevent the transfer of pollutants towards the desert plain. The easterly winds weaken, and the winds that cause pollution to transfer become very weak. The transfer towards central regions of Iran declines, and the concentrations do not increase (Figure 10_b_right).

From February 22 to 28, with the intrusion of a high-pressure system (a blocking system), the winds over the Caspian Sea shift northward again, and the concentrations increase in the sea. The transfer of pollutants continues towards lower latitudes to the north of the Lut desert,
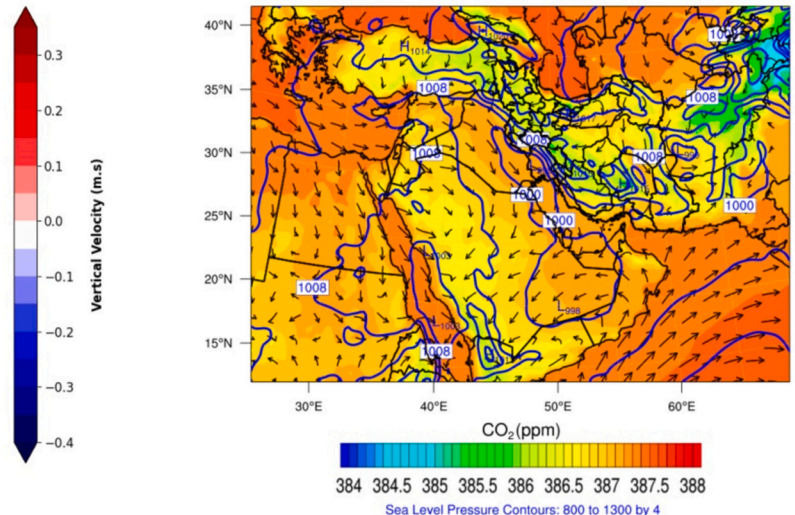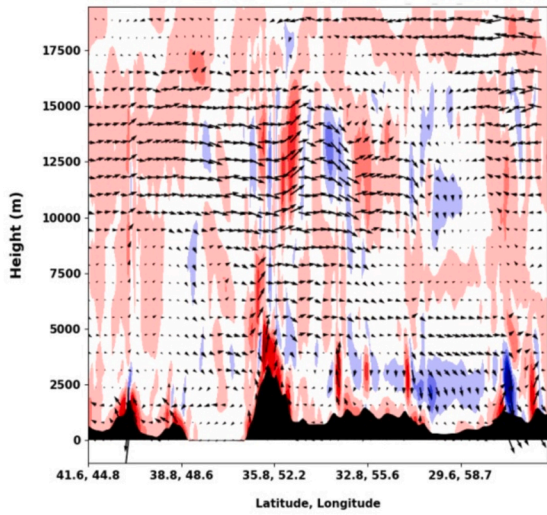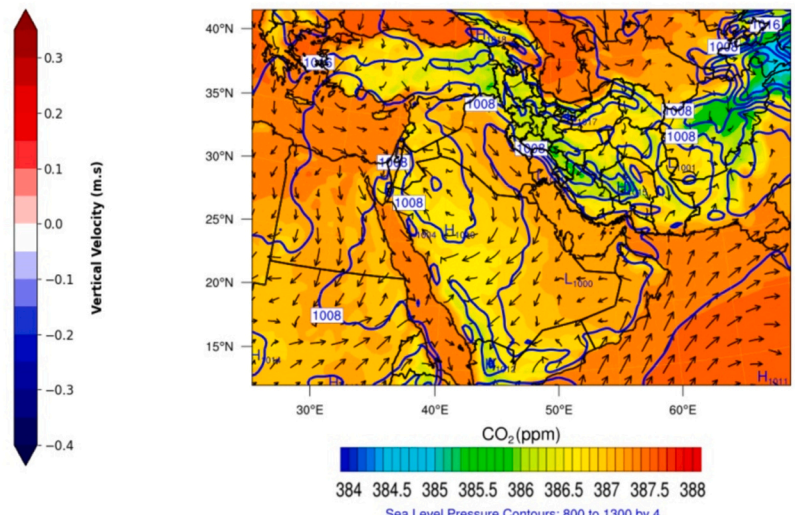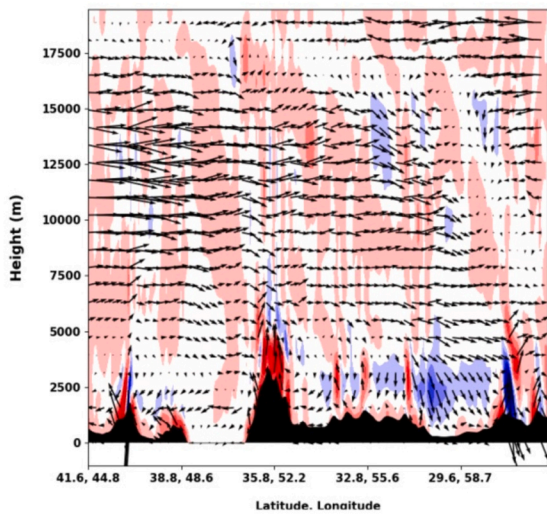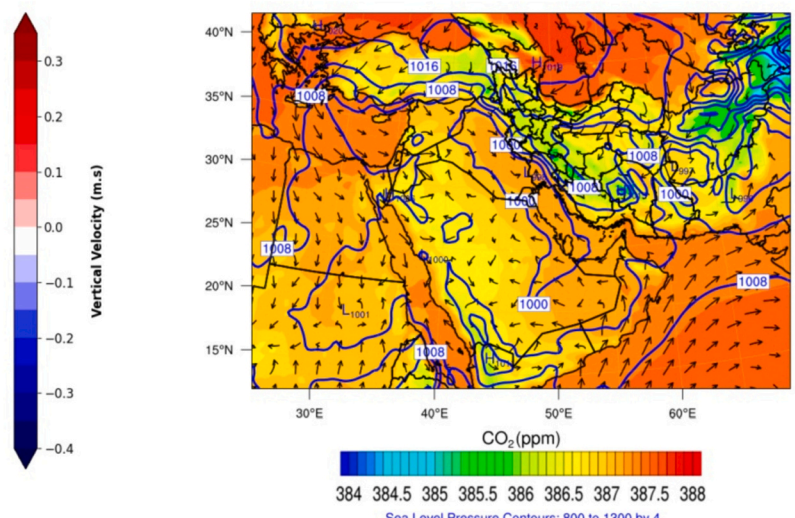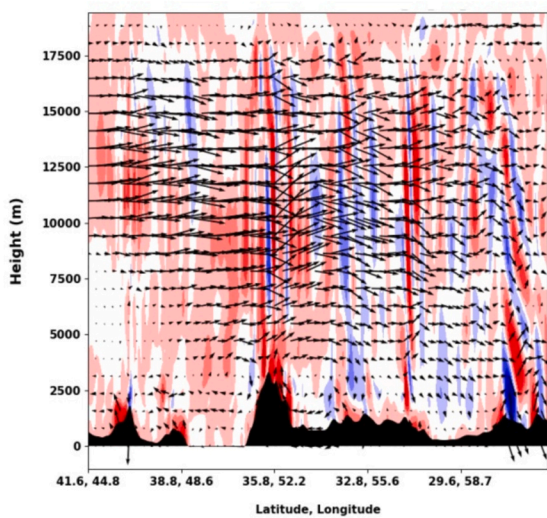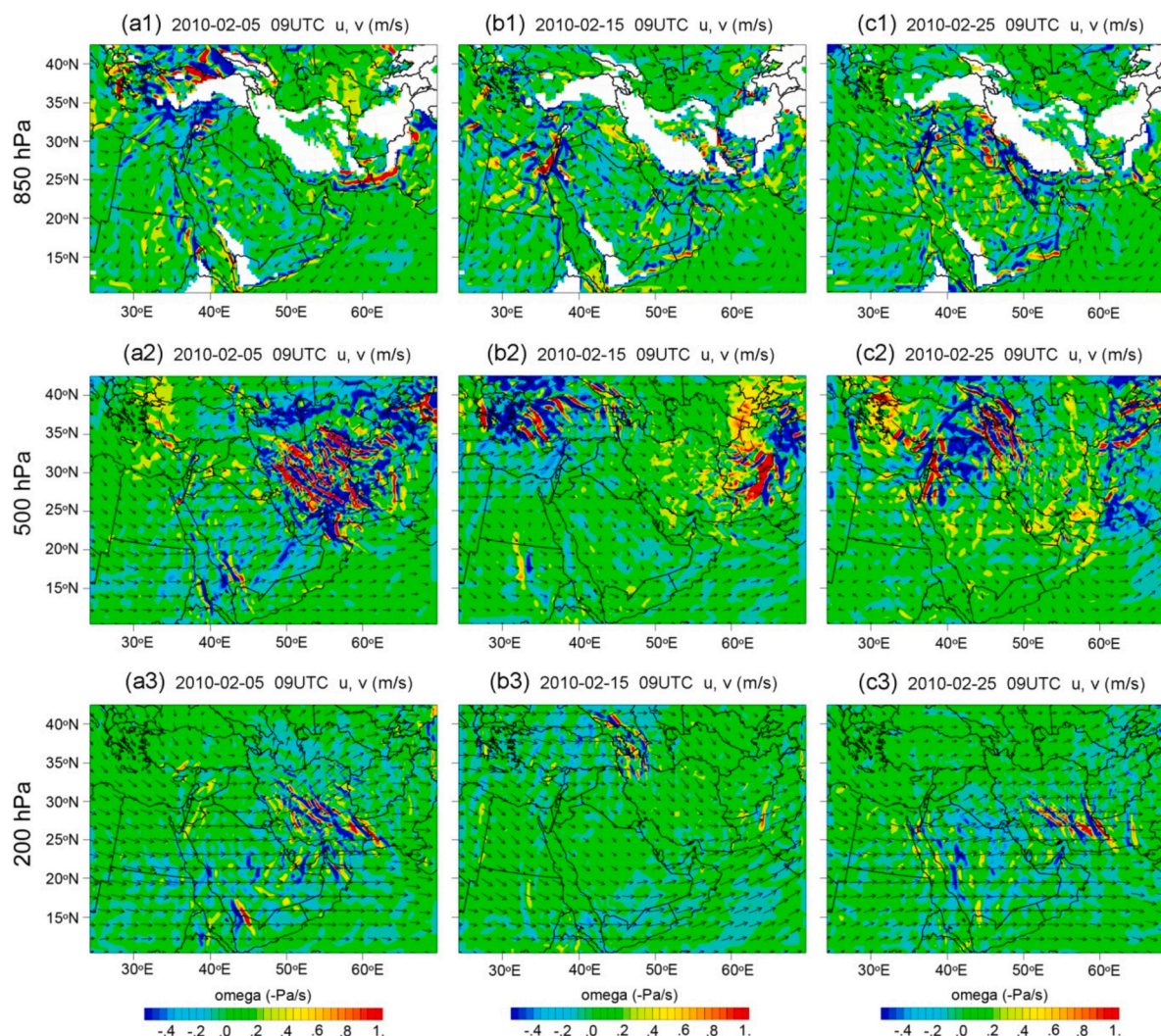
Fig. 8. Cross section along A-B of vertical velocity in color shading and (u, w) wind vectors, simulated by WRF-GHG (a,b,c_left). Spatial distribution of WRF-GHG simulations of average column CO_2 concentration (ppm) (a,b,c_right) every 10 days: August 5, 15, and 25, 2010.

Fig. 9. Omega (-Pa/s) and horizontal wind at 850 hPa, 500 hPa and 200 hPa on February 5, 15 and 25, 2010 (a, b, c). Blue (red) colors denote subsidence (ascent). (For interpretation of the references to color in this figure legend, the reader is referred to the web version of this article.)

and under these conditions, the wind direction in the Caspian regions becomes northwesterly and easterly (Figure 10_c_right).

The vertical cross sections of CO_2 concentration and wind provide additional insight into the columnar analysis. Fig. 11(a-d) shows that in February, the concentrations are higher in the troposphere, and CO_2 is advected from northern latitudes to Central Iran (on the left of the plots), crosses over the Zagros Mountains, and passes over the Persian Gulf and the Arabian Peninsula to Oman. Back trajectories calculated every 250 m from 1000 to 10,000 m asl over a point (34^{0}N, 55°E) in the Kavir plain in northern-central Iran trace back the transport at low heights to higher latitudes, to the Caspian Sea and beyond to Kazakhstan. Trajectories reaching the point at altitudes above the mid-troposphere are subsiding over the eastern Mediterranean and reside at low altitudes over Irak and the Arabian Peninsula before being uplifted when passing over the Zagros Mountains and reaching the site.

In contrast, CO_2 advection in August, Fig. 11(e-h), takes place in the lower stratosphere. The vertical cross sections show the zonal component of the wind, and the back trajectories show the meridional origin of the air flows at the highest altitude. There is also a layer with CO_2 concentrations around the middle troposphere that may extend vertically down to the Zagros Mountains. However, the summer circulations over the mountains and the heat-low over Central Iran do not favor CO_2 reaching the surface in Central Iran.

The vertically resolved plots show, in agreement with the global CO_2 column concentration (TM3 model) and our simulations (WRF-GHG), that the range of the concentrations is higher in winter and there are higher CO_2 column concentrations in northern latitudes. In contrast, in summer, CO_2 is advected from the south and concentrations are higher at lower levels.

Our results are in accordance with the study of Diallo et al. (2017) on the meridional and vertical distribution of CO_2 in the atmosphere. These authors show, for 2010 as an example, that in winter there are high concentrations at low levels in the extra tropics and that there is an inversion in the vertical profiles of CO_2 concentrations in summer time, with high concentrations in the lower stratosphere and low concentration in the troposphere, in the Northern Hemisphere. Besides the strong seasonal cycle induced by the activity in the biosphere, large-scale circulations between the tropics and the extra-tropics explain such an inversion in the vertical profile (Diallo et al., 2017).

4. Conclusions

In this study, the WRF-GHG model was used to simulate weather variables and carbon dioxide greenhouse gas concentrations in the Middle East-Iran region during February and August 2010. The simulations were performed using the GHG gas-phase chemistry scheme and the simulated column concentrations were examined using GOSAT satellite data. The significant contribution of the greenhouse gas CO_2 from
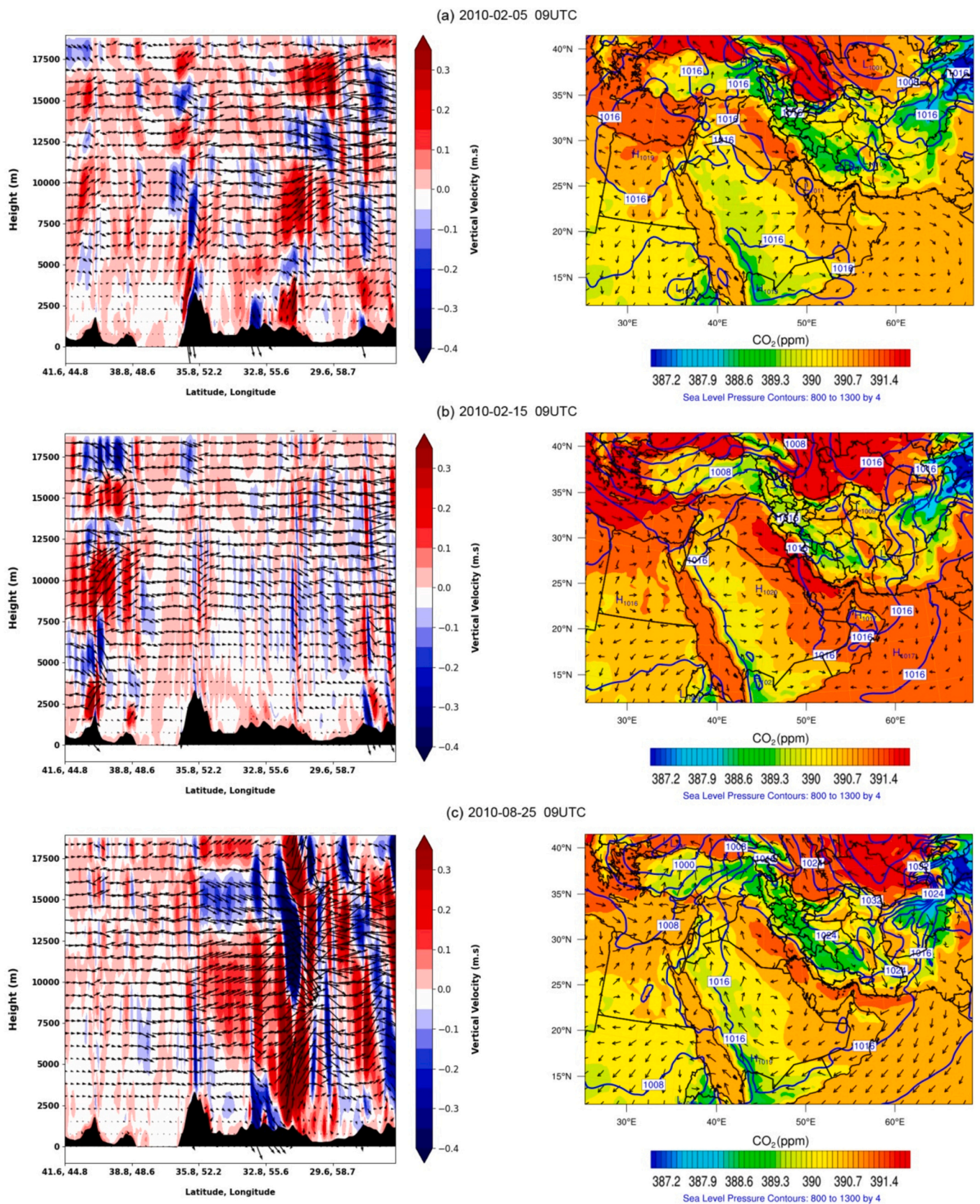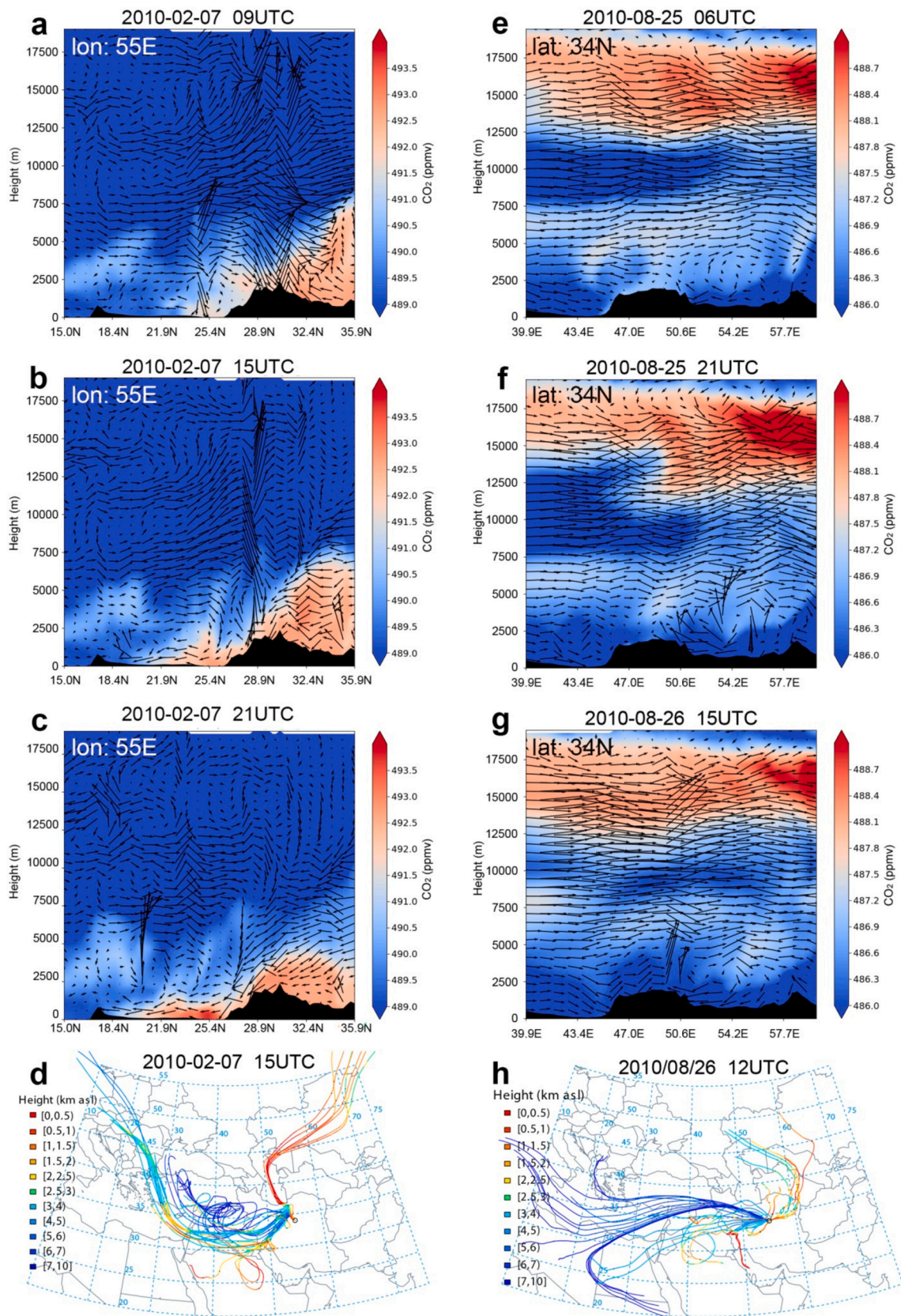
Fig. 10. Cross section along A-B of vertical velocity in color shading, and (u, w) wind vectors simulated by WRF-GHG (a,b,c_left). Spatial distribution of WRF-GHG simulations of average column CO_2 concentration (ppm) (a,b,c_right) every 10 days: February 5, 15, and 25, 2010.

Fig. 11. CO_2 and wind along vertical cross sections simulated by WRF-GHG at constant longitude 55°E (a-c) in February, and constant latitude 34°N (e-g) in August. Back trajectories calculated at different altitudes on 250 m steps from 1000 to 10,000 m over a point in the Kavir plain (d and h).

local emission sources (such as cities, power plants, etc.) was observed.

We show that the WRF-GHG model is able to reproduce temporal variations in surface temperature, relative humidity, and wind. However, this model underestimates the air temperature and relative humidity in the study area (Iran). In simulating carbon dioxide concentrations, the WRF-GHG model overestimates the CO_2 concentration compared to GOSAT satellite observations in dry months and underestimates it in wet months. The simulation errors of CO_2 can be attributed to the uncertainty in simulating different input components of the CO_2 emission inventory. Improving the simulation for various input parameters provided to the model as primary CO_2 emissions can generally help improve the CO_2 simulation. Potential sources of errors in the CO_2 components are predicted to include uncertainty in anthropogenic, biogenic, and background concentration emissions as initial conditions and boundary fields of pollutant chemistry and background values of meteorological fields, which depend on weather predictions. The uncertainty in the chemical emission simulation of the model in different locations (e.g., rural, urban, suburban), the meteorological factors that can affect the concentrations, and the need to improve weather forecasts, especially large errors in wind speed predictions, are also identified.

Wind is an important factor in the transport of pollutants and also affects other processes, such as dry deposition. Wind speed and direction errors can lead to poor representation of transport and mixing. One way to improve such simulations is to include better initial CO_2 emission rates and background CO_2 fields and use data assimilation techniques to initialize the model. Accurate emission rates are also essential for improving air quality simulations. Errors may also occur when estimating anthropogenic and biogenic emissions, which need to be minimized.

Furthermore, studying the role of atmospheric dispersion, transport, and circulation on the observed concentrations of pollutants in the central and eastern regions of Iran under the influence of wind fields shows high column concentrations of greenhouse gases in these areas during February and August. These areas are influenced both by the interaction of the heat-low with the Indian monsoon that leads to the 120-day wind system in north Sistan in the east of the country, and by the interaction of the heat-low with the Arabian high-pressure system in the west and the Zagros Mountains summer wind.

The simulated vertical cross sections of CO_2 in February and August show a distinct behavior. In February, concentrations are high in the mid-lower troposphere and are advected from the north to central Iran; on the contrary, in August, the lower stratosphere has high concentrations that are advected from the south to central Iran. The inverted CO_2 vertical profile observed at the study area is associated with reducing CO_2 close to the surface due to vegetation in summer and to seasonal large-scale circulations between the tropics and the extra tropics that involve transport between the troposphere and stratosphere.

The simulated vertical CO_2 profiles have only been partially validated by their column-averaged values in the study area. Further study of vertical profiles is relevant because the radiative effect of CO_2 is the opposite according to the sign of the vertical gradient of CO_2 in the profile, which shows a marked seasonality. Comparison of regional models such as WRF-GHG with vertically-resolved measurements, which are still limited in their spatial and temporal coverage, will improve the quantification and understanding of the CO_2 concentration in the atmosphere.

CRediT authorship contribution statement

Samira Karbasi: Writing – original draft, Visualization, Validation, Methodology, Investigation, Formal analysis, Data curation. **Amir Hossein Abdi:** Writing – review & editing, Investigation, Formal analysis, Data curation. **Hossein Malakooti:** Supervision, Methodology, Conceptualization. **Jose Antonio Garcia Orza:** Writing – review & editing, Visualization, Supervision, Investigation.

Declaration of competing interest

The authors declare that they have no known competing financial interests or personal relationships that could have appeared to influence the work reported in this paper.

Data availability

Data will be made available on request.

References

Ballav, S., Mukherjee, S., Dimri, A.P., 2020. Response of a Global Spectral Model for Simulation of Indian Summer Monsoon Rainfall. Journal of Climate Change 6 (2), 33–46.

Ballav, S., Naja, M., Patra, P.K., Machida, T., Mukai, H., 2020. Assessment of spatio-temporal distribution of CO 2 over greater Asia using the WRF–CO 2 model. Journal of Earth System Science 129, 1–16.

Barkley, M.P., Monks, P.S., Hewitt, A.J., Machida, T., Desai, A., Vinnichenko, N., et al., 2007. Assessing the near surface sensitivity of SCIAMACHY atmospheric CO 2 retrieved using (FSI) WFM-DOAS. Atmospheric Chemistry and Physics 7 (13), 3597–3619.

Beck, K.A., Joshi, P., 2015. An analysis of the environmental Kuznets curve for carbon dioxide emissions: evidence for OECD and non-OECD countries. Eur. J. Sustain. Dev. 4 (3), 33-33.

Bloom, A.A., Bowman, K.W., Lee, M., Turner, A.J., Schroeder, R., Worden, J.R., et al., 2017. A global wetland methane emissions and uncertainty dataset for atmospheric chemical transport models (WetCHARTs version 1.0). *Geoscientific Model. Development* 10 (6), 2141–2156.

Bovensmann, H., Burrows, J.P., Buchwitz, M., Frerick, J., Noel, S., Rozanov, V.V., et al., 1999. SCIAMACHY: Mission objectives and measurement modes. J. Atmos. Sci. 56 (2), 127–150.

Branch, O., Schwitalla, T., Temimi, M., Fonseca, R., Nelli, N., Weston, M., Milovac, J., Wulfmeyer, V., 2021. Seasonal and diurnal performance of daily forecasts with WRF V3.8.1 over the United Arab Emirates. Geosci. Model Dev. 14, 1615–1637. https://doi.org/10.5194/gmd-14-1615-2021.

Butz, A., Hasekamp, O.P., Frankenberg, C., Aben, I., 2009. Retrievals of atmospheric CO2 from simulated space-borne measurements of backscattered near-infrared sunlight: accounting for aerosol effects. Appl. Opt. 48 (18), 3322–3336.

Chen, F., Dudhia, J., 2001. Coupling an advanced land surface–hydrology model with the Penn State–NCAR MM5 modeling system. Part I: Model implementation and sensitivity. Monthly weather review 129 (4), 569–585.

Crippa, M., Guizzardi, D., Butler, T., Keating, T., Wu, R., Kaminski, J., et al., 2023. The HTAP_v3 emission mosaic: merging regional and global monthly emissions (2000–2018) to support air quality modelling and policies. Earth Syst. Sci. Data 15 (6), 2667–2694.

Diallo, M., Legras, B., Ray, E., Engel, A., Añel, J.A., 2017. Global distribution of CO₂ in the upper troposphere and stratosphere. Atmos. Chem. Phys. 17, 3861–3878. https://doi.org/10.5194/acp-17-3861-2017.

Dudhia, J., 1989. Numerical study of convection observed during the winter monsoon experiment using a mesoscale two-dimensional model. J. Atmos. Sci. 46 (20), 3077–3107.

EIA, 2023. Country Analysis Brief: Kuwait, July 2023. U.S. Energy Information Administration. https://www.eia.gov/international/content/analysis/countries_long/kuwait/kuwait.pdf.

Fischer, M.L., Parazoo, N., Brophy, K., Cui, X., Jeong, S., Liu, J., et al., 2017. Simulating estimation of California fossil fuel and biosphere carbon dioxide exchanges combining in situ tower and satellite column observations. J. Geophys. Res. Atmos. 122 (6), 3653–3671.

Frankenberg, C., Wunch, D., Toon, G., Risi, C., Scheepmaker, R., Lee, J.E., Wennberg, P., Worden, J., 2012. Water vapor isotopologues retrievals from high resolution GOSAT short-wave infrared spectra. Atmos. Meas. Tech. 6, 263–274. https://doi.org/10.5194/amt-6-263-201.

Grell, G.A., Dévényi, D., 2002. A generalized approach to parameterizing convection combining ensemble and data assimilation techniques. Geophys. Res. Lett. 29 (14), 38–41.

Hakkarainen, J., Ialongo, I., Tamminen, J., 2016. Direct space-based observations of anthropogenic CO₂ emission areas from OCO-2. Geophys. Res. Lett. 43 (21), 11–400.

Heimann, M., Körner, S., 2003. The Global Atmospheric Tracer Model TM3: Model Description and User Manual. Release 3.8a. Max Planck Institute for Biogeochemistry, Jena.

Hong, S.Y., Dudhia, J., Chen, S.H., 2004. A revised approach to ice microphysical processes for the bulk parameterization of clouds and precipitation. Monthly weather review 132 (1), 103–120.

Houweling, S., Breon, F.M., Aben, I., Rödenbeck, C., Gloor, M., Heimann, M., Ciais, P., 2004. Inverse modeling of CO₂ sources and sinks using satellite data: a synthetic inter-comparison of measurement techniques and their performance as a function of space and time. Atmos. Chem. Phys. 4 (2), 523–538.

Huang, K., Peng, X., Kong, L., Wu, W., Chen, Y., Maravelias, C.T., 2021. Greenhouse gas emission mitigation potential of chemicals produced from biomass. ACS Sustain. Chem. Eng. 9 (43), 14480–14487.

IPCC 2021 *Climate Change 2021: The Physical Science Basis. Contribution of Working Group I to the Sixth Assessment Report of the Intergovernmental Panel on Climate Change* ed V Masson-Delmotte *et al* (Cambridge: Cambridge University Press) Summary for policymakers accepted.

Jain, N., Bhatia, A., Pathak, H., Gupta, N., Sharma, D.K., Kaushik, R., 2015. Greenhouse gas emission and global warming. In: Introduction to Environmental Sciences, pp. 379–411.

Janjić, Z.I., 1994. The step-mountain eta coordinate model: further developments of the convection, viscous sublayer, and turbulence closure schemes. Mon. Weather Rev. 122 (5), 927–945.

Karbasi, S., Malakooti, H., Rahnama, M., Azadi, M., 2022. Study of mid-latitude retrieval X CO2 greenhouse gas: validation of satellite-based shortwave infrared spectroscopy with ground-based TCCON observations. Sci. Total Environ. 836, 155513.

Kondo, S., 2024. Kuwait's Diplomacy and the Formulation of Arab Oil Policies, 1970–1973. JIME Online Middle East Series. https://jime.ieej.or.jp/htm/extra/online_series/02_20240123.pdf.

Kuze, A., Suto, H., Nakajima, M., Hamazaki, T., 2009. Thermal and near infrared sensor for carbon observation Fourier-transform spectrometer on the greenhouse gases observing satellite for greenhouse gases monitoring. Appl. Opt. 48 (35), 6716–6733.

Liu, Y., Yue, T., Zhang, L., Zhao, N., Zhao, M., Liu, Y., 2018. Simulation and analysis of XCO2 in North China based on high accuracy surface modeling. Environ. Sci. Pollut. Res. 25, 27378–27392.

MacLeod, M.J., Hasan, M.R., Robb, D.H., Mamun-Ur-Rashid, M., 2020. Quantifying greenhouse gas emissions from global aquaculture. Sci. Rep. 10 (1), 11679.

Massart, S., Agusti-Panareda, A., Aben, I., Butz, A., Chevallier, F., Crevoisier, C., et al., 2014. Assimilation of atmospheric methane products in the MACC-II system: from SCIAMACHY to TANSO and IASI. Atmos. Chem. Phys. 14.

Meinshausen, M., Vogel, E., Nauels, A., Lorbacher, K., Meinshausen, N., Etheridge, D.M., et al., 2017. Historical greenhouse gas concentrations for climate modelling (CMIP6). Geosci. Model Dev. 10 (5), 2057–2116.

Miao, R., Lu, N., Yao, L., Zhu, Y., Wang, J., Sun, J., 2013. Multi-year comparison of carbon dioxide from satellite data with ground-based FTS measurements (2003−2011). Remote Sens. 5 (7), 3431–3456.

Miller, S.M., Wofsy, S.C., Michalak, A.M., Kort, E.A., Andrews, A.E., Biraud, S.C., et al., 2013. Anthropogenic emissions of methane in the United States. Proceedings of the National Academy of Sciences 110 (50), 20018–20022.

Mlawer, E.J., Taubman, S.J., Brown, P.D., Iacono, M.J., Clough, S.A., 1997. Radiative transfer for inhomogeneous atmospheres: RRTM, a validated correlated-k model for the longwave. J. Geophys. Res. Atmos. 102 (D14), 16663–16682.

Monin, A.S., Obukhov, A.M., 1954. Basic laws of turbulent mixing in the surface layer of the atmosphere. Geophys. Inst. Acad. Sci. 151 (163), e187.

Oshchepkov, S., Bril, A., Yokota, T., Wennberg, P.O., Deutscher, N.M., Wunch, D., et al., 2013. Effects of atmospheric light scattering on spectroscopic observations of greenhouse gases from space. Part 2: algorithm intercomparison in the GOSAT data processing for CO2 retrievals over TCCON sites. J. Geophys. Res. Atmos. 118 (3), 1493–1512.

Parker, R., Boesch, H., Cogan, A., Fraser, A., Feng, L., Palmer, P.I., et al., 2011. Methane observations from the Greenhouse gases observing SATellite: comparison to ground-based TCCON data and model calculations. Geophys. Res. Lett. 38 (15).

Patra, P., Law, R.M., Peters, W., Rödenbeck, C., Takigawa, M., Aulagnier, C., et al., 2008. TransCom model simulations of hourly atmospheric CO2: analysis of synoptic-scale variations for the period 2002–2003. Glob. Biogeochem. Cycles 22 (4).

Peng, Z., Zhang, M., Kou, X., Tian, X., Ma, X., 2015. A regional carbon data assimilation system and its preliminary evaluation in East Asia. Atmos. Chem. Phys. 15 (2), 1087–1104.

Peters, W., Jacobson, A.R., Sweeney, C., Andrews, A.E., Conway, T.J., Masarie, K., et al., 2007. An atmospheric perspective on north American carbon dioxide exchange: CarbonTracker. Proc. Natl. Acad. Sci. 104 (48), 18925–18930.

Peylin, P., Houweling, S., Krol, M.C., Karstens, U., Rödenbeck, C., Geels, C., et al., 2011. Importance of fossil fuel emission uncertainties over Europe for CO2 modeling: model intercomparison. Atmos. Chem. Phys. 11 (13), 6607–6622.

Sarrat, C., Noilhan, J., Dolman, A.J., Gerbig, C., Ahmadov, R., Tolk, L.F., et al., 2007. Atmospheric CO2 modeling at the regional scale: an intercomparison of 5 meso-scale atmospheric models. BioGeo 4 (6), 1115–1126.

Scarpelli, T.R., Jacob, D.J., Villasana, C.A.O., Hernández, I.F.R., Moreno, P.R.C., Alfaro, E.A.C., et al., 2020. A gridded inventory of anthropogenic methane emissions from Mexico based on Mexico's national inventory of greenhouse gases and compounds. Environmental Research Letters 15 (10), 105015.

Skamarock, W.C., Klemp, J.B., Dudhia, J., Gill, D.O., Liu, Z., Berner, J., et al., 2019. A Description of the Advanced Research WRF Version 4. NCAR Tech. Note NCAR/tn-556+ str, p. 145.

Solazzo, E., Crippa, M., Guizzardi, D., Muntean, M., Choulga, M., Janssens-Maenhout, G., 2021. Uncertainties in the Emissions Database for Global Atmospheric Research (EDGAR) emission inventory of greenhouse gases. Atmos. Chem. Phys. 21, 5655–5683. https://doi.org/10.5194/acp-21-5655-2021.

Taguchi, S., Law, R.M., Rödenbeck, C., Patra, P.K., Maksyutov, S., Zahorowski, W., et al., 2011. TransCom continuous experiment: comparison of 222 Rn transport at hourly time scales at three stations in Germany. Atmos. Chem. Phys. 11 (19), 10071–10084.

Takahashi, T., Sutherland, S.C., Wanninkhof, R., Sweeney, C., Feely, R.A., Chipman, D. W., et al., 2009. Climatological mean and decadal change in surface ocean p CO₂, and net sea–air CO₂ flux over the global oceans. Deep Sea Res. Part II: Top. Stud. Oceanogr. 56 (8–10), 554–577.

Tian, X., Xie, Z., Liu, Y., Cai, Z., Fu, Y., Zhang, H., Feng, L., 2014. A joint data assimilation system (Tan-Tracker) to simultaneously estimate surface CO2 fluxes and 3-D atmospheric CO2 concentrations from observations. Atmos. Chem. Phys. 14 (23), 13281–13293.

Tolk, L.F., Meesters, A.G.C.A., Dolman, A.J., Peters, W., 2008. Modelling representation errors of atmospheric CO 2 mixing ratios at a regional scale. Atmos. Chem. Phys. 8 (22), 6587–6596.

Tramontana, G., Jung, M., Schwalm, C.R., Ichii, K., Camps-Valls, G., Ráduly, B., et al., 2016. Predicting carbon dioxide and energy fluxes across global FLUXNET sites with regression algorithms. Biogeosciences 13 (14), 4291–4313.

Turner, A.J., Jacob, D.J., Wecht, K.J., Maasakkers, J.D., Lundgren, E., Andrews, A.E., et al., 2015. Estimating global and north American methane emissions with high spatial resolution using GOSAT satellite data. Atmos. Chem. Phys. 15 (12), 7049–7069.

Tyrlis, E., Lelieveld, J., 2013. Climatology and dynamics of the summer Etesian winds over the eastern Mediterranean. J. Atmos. Sci. 70 (11), 3374–3396.

Verkaik, J., 2019. Evaluation of Colombian Methane Emissions Combining WRF-Chem and TROPOMI. Master's thesis,. University of Wageningen. https://edepot.wur.nl/496227.

Vogel, F.R., Thiruchittampalam, B., Theloke, J., Kretschmer, R., Gerbig, C., Hammer, S., Levin, I., 2013. Can we evaluate a fine-grained emission model using high-resolution atmospheric transport modelling and regional fossil fuel CO2 observations? Tellus Ser. B Chem. Phys. Meteorol. 65 (1), 18681.

Wang, Y., Lü, D., Li, Q., Duan, M., Hu, F., Hu, S., 2014. Observed and simulated features of the CO2 diurnal cycle in the boundary layer at Beijing and Hefei, China. Chin. Sci. Bull. 59, 1529–1535.

Wang, P., Stammes, P., Mueller, R., 2011. Surface solar irradiance from SCIAMACHY measurements: algorithm and validation. Atmospheric Measurement Techniques 4 (5), 875–891.

WATER, W. C., 2019. *WMO greenhouse gas bulletin*.

Xie, S.P., Lu, B., Xiang, B., 2013. Similar spatial patterns of climate responses to aerosol and greenhouse gas changes. Nature Geoscience 6 (10), 828–832.

Yokota, T., Yoshida, Y., Eguchi, N., Ota, Y., Tanaka, T., Watanabe, H., Maksyutov, S., 2009. Global concentrations of CO_2 and CH_4 retrieved from GOSAT: first preliminary results. Sola 5, 160–163.

Yoshida, Y., Ota, Y., Eguchi, N., Kikuchi, N., Nobuta, K., Tran, H., et al., 2011. Retrieval algorithm for CO2 and CH4 column abundances from short-wavelength infrared spectral observations by the Greenhouse gases observing satellite. Atmos. Meas. Tech. 4 (4), 717–734.